



# PLUME-MoM-TSM 1.0.0: A volcanic columns and umbrella cloud spreading model

Mattia de' Michieli Vitturi<sup>1</sup> and Federica Pardini<sup>1</sup>

<sup>1</sup>Istituto Nazionale di Geofisica e Vulcanologia, Sezione di Pisa, Pisa, Italy

**Correspondence:** Mattia de' Michieli Vitturi (mattia.demichielivitturi@ingv.it)

## Abstract.

In this paper a new version of the integral model for volcanic plumes PLUME-MoM is presented. The model describes the steady-state dynamics of a plume in a 3-D coordinate system, and the two-size moment (TSM) method is adopted to describe changes in grain-size distribution along the plume, associated with particle loss from plume margins and with particle aggregation. For this reason, the new version is named PLUME-MoM-TSM. For the first time in a plume model, the full Smoluchowski coagulation equation is solved, allowing to quantify the formation of aggregates during the rise of the plume. In addition, PLUME-MOM-TSM allows to model the phase change of water, which can be either magmatic, added at the vent as liquid from external sources, or incorporated through ingestion of moist atmospheric air. Finally, the code includes the possibility to simulate the initial spreading of the umbrella cloud intruding from the volcanic column into the atmosphere. A transient shallow water system of equations models the intrusive gravity current, allowing to compute the upwind spreading.

The new model is applied first to the eruption of Calbuco volcano in southern Chile in April 2015, and then to a sensitivity analysis of the upwind spreading of the umbrella cloud to mass flow rate and meteorological conditions (wind speed and humidity). This analysis provides an analytical relationship between the upwind spreading and some characteristic of the volcanic column (height of the neutral buoyancy level and plume bending), which can be used to better link plume models and volcanic-ash transport and dispersion models.

## 1 Introduction

In the last years, the simulation of ash dispersal in the atmosphere has become an ordinary activity for volcanic observatories and meteorological offices. Volcanic ash represents one of the major hazard associated with explosive eruptions, affecting both the zones proximal to the volcanic vent, where it can damage vegetation, infrastructures and pose a health risk to people, and the surrounding atmosphere, requiring effective and prompt actions to regulate flights near to the ash plume (Bonadonna et al., 2020).



In order to properly model the transport of ash and its associated deposition on the ground, it is important to provide the correct inputs to volcanic-ash transport and dispersion (VATD) models, and so far the best approach has been to use the output of numerical models simulating the rise of volcanic columns up to the neutral buoyancy level, where ash clouds transported by the wind spread in the atmosphere. Column models can be broadly categorized in two classes: one-dimensional (1D) integral models (Bursik, 2001; Mastin, 2007; Degruyter and Bonadonna, 2012; Devenish, 2013; Woodhouse et al., 2013; de' Michieli Vitturi et al., 2015; Folch et al., 2016) and three dimensional (3D) models (Oberhuber et al., 1998; Suzuki and Koyaguchi, 2009; Cerminara et al., 2015; Ongaro et al., 2007). A recent inter-comparison exercise (Costa et al., 2016) has shown that 1D and 3D models, notwithstanding the formulations are different, produce consistent predictions of some of more relevant quantity describing volcanic plumes, as for example the neutral buoyancy level. For this reason, in operative contexts where multiple scenarios have to be considered and the simulation time is an important constrain, 1D models are still preferred. This class of models is based on the theory of turbulent buoyant plumes, as introduced by Morton et al. (1956), and it has been first applied in the volcanic context by Sparks (1986) and Woods (1988), which modeled the rising plume as an homogeneous mixture of gas and ash particles. Other works incorporated additional processes, such as the effects of moisture (Woods, 1993; Mastin, 2007) and ambient wind (Bursik, 2001).

Despite the relatively high number of integral model developed in the past couple of decades, some important features of volcanic plumes have been neglected so far, or they have not been considered together in a single model. Most notably, only a few models accounts for the thermodynamic phase relations for water (Herzog et al., 1998). As pointed out in several works (Koyaguchi and Woods, 1996; Woods, 1993; Sparks et al., 1997; Mastin, 2007), the presence of water, coming both from entrainment during some Surtseyan eruptions (Þórarinnsson, 1967) or from entrainment of water-saturated air (Graf et al., 1999), and the thermodynamics of condensation and evaporation, can strongly affect the rise and collapse of strong volcanic plumes. Conversely, in Woodhouse et al. (2013) it is shown that for small weak plumes, the effect on height of external humidity entrained in the eruption column is almost negligible when compared to the role played by the uncertainty in parameters like source buoyancy flux, atmospheric stratification, and wind.

Another process that is frequently disregarded in the modeling of volcanic plumes is ash particle aggregation (Brown et al., 2012). So far, the number of works describing quantitatively the aggregation processes in eruption column is quite limited (Veitch and Woods, 2001; Textor et al., 2006b, a; Brown et al., 2012; Folch et al., 2016; Künzli et al., 2018; Rossi et al., 2018). This is because this process is quite complex, from a physical point of view but also from the model perspective, requiring a careful treatment of the evolving grain size distribution. In fact, aggregation leads to the formation, from fine ash, of coarser particles, resulting in larger settling velocity than the primary particles and thus with an increased fallout of fine ash from the plume margins. A proper treatment of aggregation is thus important to predict the effective grain size distribution of ash particles reaching the neutral buoyancy level and then advected by the wind into the atmosphere.

For sustained eruptions, when neutral buoyancy level is reached, the eruptive mixture still has a vertical momentum, allowing the column to further rise and then to collapse as a gravity current spreading into the atmosphere (see Fig. 1). During the eruption of Mount St. Helens on May 18, 1980, this phenomenon was clear and satellite data were used by Sparks (1986) to validate a simple model of umbrella spreading based on continuity of mass flow rate. For large mass eruption rates this



**Figure 1.** 4 December 2015 paroxysm plume from Voragine crater at Mt. Etna, as viewed from Cesarò (Messina) at 9:27GMT. Photo by G. Famiani. The volcanic column rises vertically and then spread horizontally at the neutral buoyancy level in all the directions.

spreading can lead to an important radial expansion, including upwind transport, which is sometime omitted in numerical simulations by the simple coupling column models with VATD models. In Costa et al. (2013), an analytical model describing the spreading of the umbrella cloud as a gravity current was coupled with an advection-diffusion-sedimentation model, and the conditions under which gravity-driven transport were analyzed. Baines (2013) studied the dynamics of this gravitational spreading into a density-stratified crossflow, deriving a semi-analytic model able to produce a good description of the behaviour of the ash cloud within the vicinity of intrusion from the column. A different approach to model the spreading of the umbrella cloud is presented in Johnson et al. (2015) where, following the work of Ungarish and Huppert (2002), the flow is modeled as a transient shallow-layer gravity current subject to gravitational forces and drag between the current and the surrounding atmosphere. The results of Johnson et al. (2015) show that the current spreads in a different way from what was suggested by simple scaling arguments in previous works, such as those of Costa et al. (2013). The same approach is used in Pouget et al. (2013), where the results of a "shallow-water" model are compared with satellite observations, in order to estimate growth rates and mass fluxes. More recently, Folch et al. (2016) adopted a simple semi-empirical model to describe the umbrella region, and



70 their results are qualitatively consistent with the results obtained with more complex 3D numerical codes (Costa et al., 2016). A simple approach is also presented in Webster et al. (2020), where a parameterisation is used to model the lateral spread of the umbrella and to correct the initial conditions for transport and dispersion in the Lagrangian model NAME, resulting in substantial improvements to ash cloud predictions from large explosive eruptions.

In this work, we extend the original PLUME-MoM model, which is the first volcanic plume model based on the method of  
75 moments for the description of the polydispersity in ash particles, by adding all the important features described above: phase transition of water, particle aggregation and umbrella cloud spreading. The model is first applied to the April 2015 Calbuco eruption, by comparing simulation results with observations to constrain some model parameters. Then, a sensitivity analysis is performed with the newly developed model, in order to obtain a relationship first between eruption parameters and the upwind spreading of the umbrella cloud first, and then between the latter and other parameters characterizing the plume.

## 80 2 Model equations

In this section we present the equations solved by PLUME-MoM-TSM. First of all, the new formulation for the description of the particle size distribution, based on the method of moments, is presented in Section 2.1. Then, in Section 2.2, the steady transport equations for the plume are derived from conservation principles (mass, momentum and energy). The equations for the phase transition of water and the shallow-water equations describing the spreading of the umbrella cloud are finally  
85 presented in Sections 2.3 and 2.4, respectively.

### 2.1 Ash particle number density function

As previously stated, particle aggregation is a complex process and its modeling requires an accurate description of the particle size distribution within a column and of its changes during the rise of the volcanic mixture. While particle fallout from the plume margin changes the size distribution, but does not modify the size spectrum, aggregation leads to the formation of coarser  
90 particles, whose size was not present in the initial size distribution erupted at the vent. Furthermore, when a discretization in bins is employed to describe the variability in size, computational problems arise in the modeling of aggregation processes, because particles belonging to two bins of the original distribution could form an aggregate whose size is not represented in the chosen discretization. In this work, we try to solve these problems in the description and modeling of polydispersity in size of ash particles by adopting the method of moments.

95 In the first version of PLUME-MoM (de' Michieli Vitturi et al., 2015), the quadrature method of moments (QMOM) was used to model the polydispersity of ash particles. According to the QMOM (Marchisio et al., 2003; Marchisio and Fox, 2013; Colucci et al., 2017), the particle size distribution is approximated from the moments as a sum of Dirac delta functions, which is particularly convenient for evaluating the integrals appearing in the closure terms of the moments transport equations. When aggregation processes are considered, QMOM provides an effective alternative to the sectional (or "discrete") method, where  
100 the size spectrum is partitioned in discrete bins. Its advantages are a limited number of variables and the dynamic calculation of the more representative sizes within the distribution. The main disadvantage is that, given the moments of a distribution, it is



not possible to retrieve the amount of mass associated to a size interval. This represents a problem when the output of a plume model is used as input of a model for transport and deposition of ash in the atmosphere.

To cope with this problem, we describe here a hybrid method combining the advantages of the sectional and moment methods. With this hybrid approach, the size spectrum is still partitioned in sections (or bins), and then the transport equations for a limited number of moments for each section are solved. The number density function (NDF) is then represented by using a piecewise reconstruction, continuous on each section. Among these hybrid methods, in several engineering context, like spray modeling, the two-size moment (TSM) method has proven to produce good results for size reduction simulations (i.e. evaporation) and for coalescence, by using in each section a second-order accurate reconstruction of the NDF from the moments (Nguyen et al., 2016), leading also to a good representation of the NDF with a small number of sections. For this reasons, TSM is a good candidate for the modeling of the aggregation processes occurring in the volcanic column. In this paper, we introduce a modified version of the TSM method presented in Nguyen et al. (2016). While in the original formulation the internal variable is the volume (or the radius) of the particles and in each section the NDF is reconstructed with a linear function, here the NDF is defined as a function of particle mass. This greatly simplify the formulation when aggregation is considered (two particles of mass  $M_1$  and  $M_2$  respectively aggregate in a new particle of mass  $M = M_1 + M_2$ ). In addition, while in Nguyen et al. (2016) for some section the support of the linear reconstruction (the subset of the section containing the elements which are not mapped to zero) can be smaller than the section width (which means that the existing particles size spectrum do not cover entirely the respective section), here in those section we switch from a linear reconstruction to a power law, with zero value at one of the boundaries of the section. The advantages of this different approach will be explained in details in the following of the section.

The starting point of the TSM method is the partition of the size spectrum in  $n$  sections (or bins). Here, we use a uniform partition  $\phi_i = \phi_0 + i\Delta\phi$ ,  $i = 0, \dots, n_s$ , in the non-dimensional Krumbein  $\phi$  scale:

$$\phi = -\log_2 \frac{1000 \cdot D}{D_0}, \quad (1)$$

where  $D$  is the diameter of the particle expressed in meters, and  $D_0$  is a reference diameter, equal to 1 mm (to make the equation dimensionally consistent). Given the particles density  $\rho = \rho(\phi)$  and their sphericity, it is possible to associate to each size of the original partition  $\phi_i$  the corresponding mass particle  $m_i$ , and thus to obtain a partition of the particles mass spectrum in  $n$  sections corresponding to the  $n$  bins in the Krumbein scale. In this way, the internal variable characterizing the variability of the particle population becomes the mass, and its variability can be characterized by the ash particles number density function, here denoted by

$$\eta(m, x, t). \quad (\text{Number Density Function, NDF}) \quad (2)$$

This function represents the number of ash particles per unit volume of the gas-particle mixture in the infinitesimal mass interval  $[m; m + dm]$  at the location  $x$  in space and at the time  $t$  (according to this definition, the number density function  $\eta(m, x, t)$  has units  $L^{-3}M^{-1}$ ). With this choice, when we integrate the number density function in a fixed control volume  $V$  and over a mass interval  $[m_1; m_2]$ , we obtain the number of particles in  $V$  at time  $t$  with mass between  $m_1$  and  $m_2$ .



135 We introduce the following notation for the  $j$ -th moment of the mass distribution  $\eta$ :

$$m^{(j)} = \int_0^{+\infty} \eta(m, x, t) m^j dm. \quad [L^{-3} M^j] \quad (3)$$

One important property of the NDF adopted is that the moments of the distribution correspond to quantities that have meaningful physical interpretations and are therefore, at least in principle, directly measurable in the field, as well as in experiments. For example, we observe that the moment of order zero,  $m^{(0)}$ , represents the total number of ash particles per unit volume of the mixture, while the moment of order one,  $m^{(1)}$ , represents the total mass of ash particles per unit volume of the gas-particle mixture, i.e. the bulk density of the ash particles, here denoted with  $\rho_p^B$ . From a physical point of view, these moments are commonly the main variables of interest, since when there is no aggregation the global moment of order 0 is conserved, while with aggregation the global moment of order 1 is conserved. In addition, dividing the first moment by the average ash particle density, we obtain the volume fraction of particles with respect to the volume of the gas-particle mixture.

145 As previously stated, the mass spectrum is partitioned in  $n$  sections, and we can define the local moments of order zero and one on the  $k$ -th section defined by the mass interval  $[m_{k-1}, m_k]$ :

$$N_k(x, t) = \int_{m_{k-1}}^{m_k} \eta(m, x, t) dm, \quad M_k(x, t) = \int_{m_{k-1}}^{m_k} \eta(m, x, t) m dm. \quad (4)$$

Also in this case, the local moments have an important physical interpretation. In fact, the local moments of order one  $M_k$ ,  $k = 1, \dots, n$ , represent the mass within each mass section per unit volume of the mixture and thus, when normalized, they give the total grain size distribution. Solving for appropriate transport equation of the moments  $M_k$  allows then to describe the evolution of the total grain size distribution within the plume. We observe that, differently from the global moment of order one, the local moments of order one are not conserved by aggregation, because mass moves from sections corresponding to finer particles to sections corresponding to coarser ones.

155 The local moments of other quantities  $\psi(m)$  which depend on the mass of the particles, as for example the density, or the settling velocity, can be defined in terms of the continuous distribution of mass fraction  $\eta(m)$  as

$$\psi_k^{(i)} = \frac{1}{m^{(i)}} \int_{m_{k-1}}^{m_k} \psi(m) m^i \eta(m) dm. \quad (5)$$

This term has the same units of  $\psi(m)$  and represents its integral average, weighted differently according to the order of the moment. For example  $\psi_k^{(0)}$  represents the average of  $\psi$  in the mass interval  $[m_{k-1}, m_k]$  weighted with the number of ash particles of different masses, while  $\psi_k^{(1)}$  represents a mass-weighted average in the same interval.

160 When the moments of the mass distribution  $\eta$  are known for each section, but not the actual expression of  $\eta$ , the integral in Eq. (5) must be approximated with a quadrature formula, and to do this we need the "weights" and the "nodes" (or "abscissae") of the quadrature. Here, we use an approach based on the Gauss-Legendre quadrature, which can be written as

$$\int_{-1}^1 f(x) dx \approx \sum_{i=1}^n \omega_i f(x_i) \quad (6)$$



where the  $i$ -th node  $x_i$  is the  $i$ -th root of the Legendre polynomial  $P_n(x)$  and the weights  $\omega_i$  are given by the Abramowitz-  
 165 Stegun 1972 formula (Abramowitz and Stegun, 1965). This  $n$ -points quadrature formula is exact for polynomials of degree  
 $2n - 1$  or less. From these quadrature nodes and weights defined for the standard interval  $[-1; 1]$ , it is possible to compute the  
 nodes and weights for the integral over the interval  $[m_{k-1}, m_k]$ :

$$\int_{m_{k-1}}^{m_k} f(x) dx \approx \sum_{i=1}^n \tilde{\omega}_{k,i} f(\tilde{x}_{k,i}) \quad (7)$$

where

$$170 \quad \tilde{\omega}_{k,i} = \frac{m_k - m_{k-1}}{2} \omega_i \quad \tilde{x}_{k,i} = \frac{m_k - m_{k-1}}{2} x_i + \frac{m_{k-1} + m_k}{2}. \quad (8)$$

With this approach, when the integrand of Eq. (5) changes (for example because the mass distribution changes in space  
 or time), there is no need to reevaluate the quadrature nodes and weights, which depends only on the interval and can be  
 computed in advance. The only thing to update is the value of the integrand at the quadrature points. In the TSM approach, as  
 presented in Nguyen et al. (2016), mass distribution  $\eta(m)$  is approximated in each section by a linear function. Here, non-linear  
 175 approximations  $\approx \tilde{\eta}_k(m)$  of the mass distribution are considered. On each section  $k$ , a continuous reconstruction is assumed:

$$\eta(m)|_{m \in [m_{k-1}, m_k]} = \eta_k(m) \approx \tilde{\eta}_k(m) \quad (9)$$

where three possible continuous reconstructions are used for each  $\tilde{\eta}_k(m)$ , as illustrated in Fig. 2:

$$\tilde{\eta}_k(m) = \begin{cases} \left[ \beta_k \left( \frac{m - m_{k-1}}{m_k - m_{k-1}} \right)^{\gamma_k} \right] \mathbf{1}_{[m_{k-1}, m_k]}(m) & \text{CASE 1} \\ \left[ \alpha_k + (\beta_k - \alpha_k) \frac{m - m_{k-1}}{m_k - m_{k-1}} \right] \mathbf{1}_{[m_{k-1}, m_k]}(m) & \text{CASE 2} \\ \left[ \alpha_k \left( \frac{m_k - m}{m_k - m_{k-1}} \right)^{\gamma_k} \right] \mathbf{1}_{[m_{k-1}, m_k]}(m) & \text{CASE 3} \end{cases} \quad (10)$$

The parameters  $\alpha_k, \beta_k$  (representing the values of the reconstructed function at  $m_{k-1}$  and  $m_k$ ) and  $\gamma_k$  are computed in order  
 180 to have

$$\tilde{\eta}^{(0)} = N_k, \quad \tilde{\eta}^{(1)} = M_k. \quad (11)$$

In this way, the domain of each function  $\tilde{\eta}_k(m)$  is always the whole  $k$ -th section, and there is no need to update the quadrature  
 nodes.

So far we presented the TSM approach for a single family of particles. When more than one particle family is considered, for  
 185 example if we consider aggregation and we want to distinguish between aggregated and non-aggregated particles, the subscript  
 $i_p$  is used to distinguish the mass distribution functions  $\eta_{i_p}(m, x, t)$ ,  $i_p = 1, \dots, n_p$ , where  $n_p$  is the number of particles  
 families. Similarly, the notation  $m_{i_p}^{(j)}$  is introduced for the  $j$ -th moment of the  $i_p$ -th distribution, and the notations  $N_{i_p, k}$  and  
 $M_{i_p, k}$  for the number and mass of particles of the  $i_p$ -th family in the  $k$ -th section, respectively.

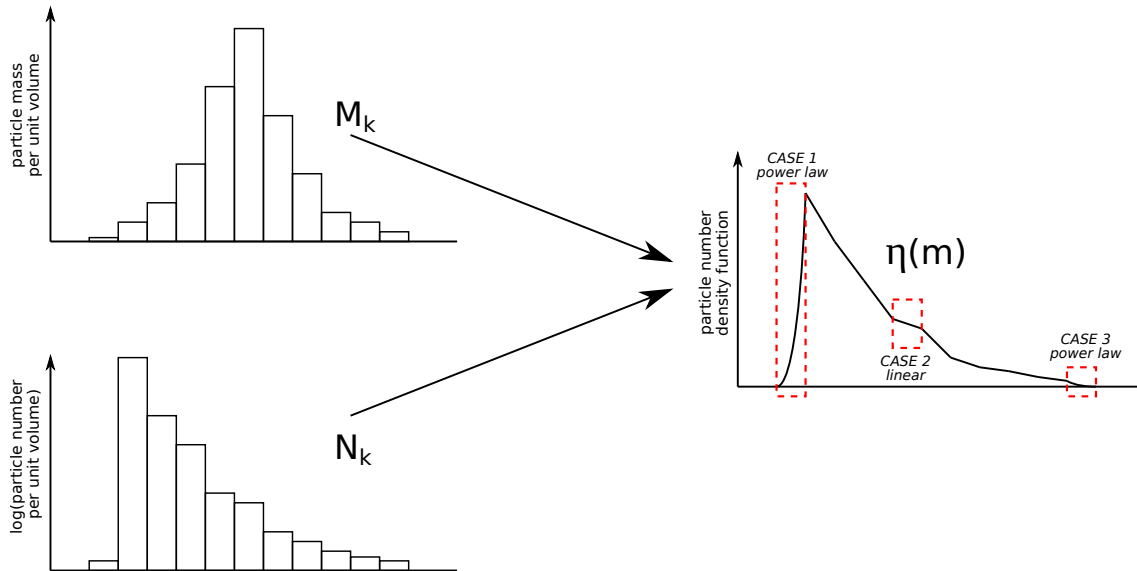


**Figure 2.** Piecewise reconstruction of the number density function from the local moments. The values of the first two moments in each section (plotted on the two bar plots on the left) are used for the reconstruction of the piecewise continuous density function. The function is linear in the internal sections and a power law at the boundaries.

## 2.2 Plume equations

190 In this section we present the set of conservation equations describing the steady rise ( $d/dt = 0$ ) of the volcanic mixture through the atmosphere. As in Bursik (2001), the model assumes a homogeneous mixture of different phases with thermal and mechanical equilibrium between all of them. In this version of the model, in addition to air and particles, we also explicitly model the presence of water, which can be in gas, liquid or solid state, and the presence of additional volcanic gases (transported as passive components). The equation set for the plume rise model is solved in a 3-D coordinate system  $(x, y, z)$  centered horizontally at the plume base location, and vertically at the sea level. The plume is assumed with a circular section with radius  $r$ , parallel to the horizontal plane  $(x, y)$  and orthogonal to the vertical coordinate  $z$  (see Fig. 3).

195

In the  $(x, y, z)$  coordinate system, we denote with  $u$ ,  $v$  and  $w$  the three components of plume velocity, and with  $U_{sc} = \sqrt{u^2 + v^2 + w^2}$  its magnitude. Furthermore, we define  $\phi$  as the angle between the axial direction and the horizontal plane, for which it holds the following relationship

$$200 \quad \tan \phi = \frac{w}{\sqrt{u^2 + v^2}}.$$

We also consider the presence of an horizontal atmospheric wind, with velocity components  $u_a$ ,  $v_a$  and magnitude  $U_{atm}$ . Because of the wind, the location of the centers of the horizontal section, which defines the plume center-line, can be bent.

The rising multiphase mixture is formed by different families of solid particles (differing in shape, density, thermal properties), dry air, water (which can be in vapour, liquid and ice form) and other volcanic gases, such as  $\text{CO}_2$  and  $\text{SO}_2$ . When

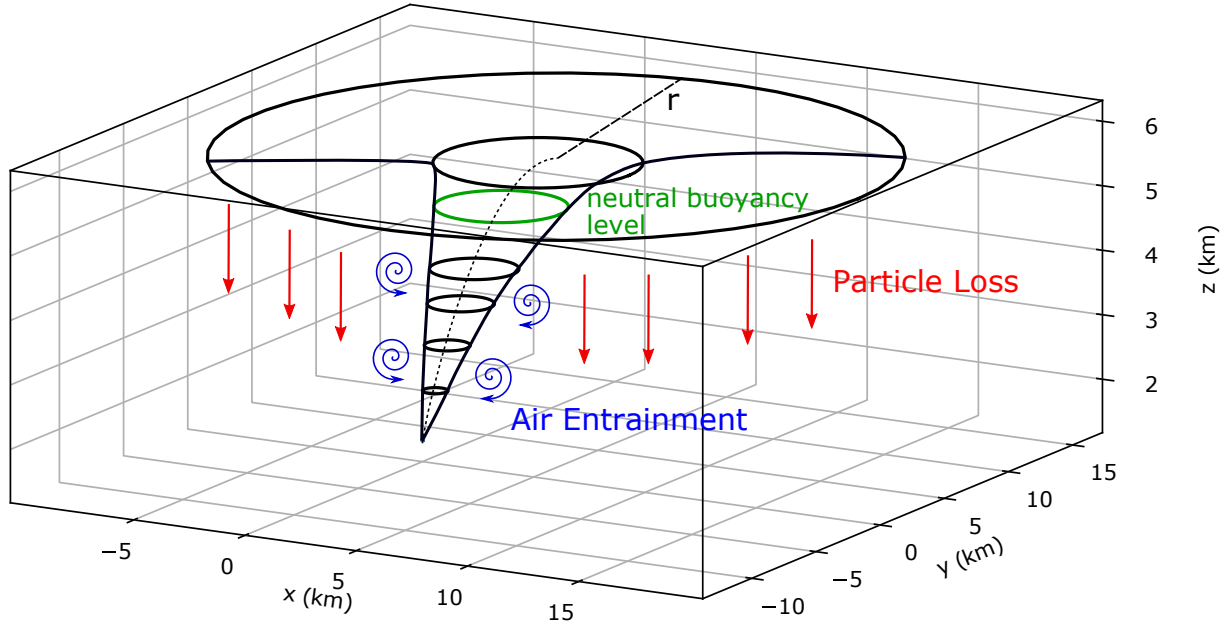


**Figure 3.** Schematic view of the plume. The dashed line represents the centerline of the plume. The horizontal circles are the section over which plume variables are averaged. The green circle represents the plume section at the neutral boundary level.

205 more than one particle family is considered, they are denoted with the subscript  $i_p = 1, \dots, n_p$ ; in addition, if aggregation is considered, we use the first  $n_p - 1$  indexes for the original particles and the last one for the aggregated particles. With this notation, for the particles with mass  $m$  of the family  $i_p$ , we can write the following equation for the vertical mass flux through an horizontal cross-section of the plume (see Fig. 3):

$$\frac{d}{dz} (\eta_{i_p}(m, z) \pi r^2 w) = -2\pi r p w_{i_p}(m) \cdot \eta_{i_p}(m, z) + S_{i_p}, \quad (12)$$

210 where both the plume radius  $r$  and the vertical component of the plume axial velocity  $w$  vary with the vertical coordinate  $z$ . Equation (12) describes the variation with the vertical coordinate  $z$  of the mass flux of particles of size  $m$ , due to fallout of pyroclasts (first term on the right-hand side) and aggregation (second term on the right hand side). Here,  $w_{i_p}(\cdot)$  is the particle settling velocity (see Appendix A2) and the coefficient  $p$ , which is a function of the radial entrainment coefficient  $\alpha$ , expresses the probability that an individual particle will fall out of the plume:

$$215 \quad p = \frac{\left(1 + \frac{6}{5}\alpha\right)^2 - 1}{\left(1 + \frac{6}{5}\alpha\right)^2 + 1}. \quad (13)$$



The last term on the right hand side of Eq. (12) represents the aggregation term which, following Von Smoluchowski, can be written as:

$$S_{i_p}(m, z) = -\pi r^2 \sum_{l_p=1}^{n_p} \left( \eta_{i_p}(m, z) \int_0^{+\infty} \beta(z, m, m') \eta_{l_p}(m', z) dm' \right) \quad i_p = 1, \dots, n_p - 1 \quad (14)$$

$$S_{n_p}(m, z) = \pi r^2 \sum_{l_p=1}^{n_p} \left( \sum_{k_p=1}^{n_p} \frac{1}{2} \int_0^m \beta(z, m - m', m') \eta_{l_p}(m - m', z) \eta_{k_p}(m', z) dm' \right. \\ \left. - \eta_{n_p}(m, z) \int_0^{+\infty} \beta(z, m, m') \eta_{l_p}(m', z) dm' \right) \quad (15)$$

220

where  $\beta(z, m, m')$  is the aggregation (or coagulation) kernel describing the rate at which a particle of mass  $m$  aggregate with a particle of mass  $m'$ . The equations state that the aggregation of particles of mass  $m$  and  $m'$ , forming a particle of size  $m + m'$ , is proportional to the number density of particles of such masses ( $\eta(m)$  and  $\eta(m')$ ) and to the aggregation kernel. The negative term on the right hand side of the first equation represents the loss of ash particles of the original families due to aggregation. The positive term on the right hand side of second equation represents the increase of particles of mass  $m$  at the vertical coordinate  $z$  due to aggregation of smaller particles. The aggregation kernel can be defined as the product of two quantities: the "collisions frequency" between particles of mass  $m$  and  $m'$  and the "efficiency of aggregation" (i.e., the probability of particles of mass  $m$  coalescing with particles of mass  $m'$  when colliding). In PLUME-MoM-TSM several aggregation kernel are implemented, from simple constant kernels to more complex formulations describing wet aggregation, where the collisions frequency depends on particles properties (size, density) and the efficiency of aggregation depends on the amount of water in the mixture (see Appendix A3).

225

230

Let us consider now a mass interval  $\Omega$ , which can be the whole ash particle mass spectrum or a smaller subset, as the  $k$ -th section for the family  $i_p$ , defined by  $[m_{i_p, k-1}; m_{i_p, k}]$ . Multiplying Eq. (12) for  $m^i$  and integrating over  $\Omega$ , we obtain the following differential equations for the moments:

235

$$\frac{d}{dz} (m_{i_p}^{(i)} w r^2) = -2r p w_{i_p}^{(i)} m_{i_p}^{(i)} + \hat{S}_{i_p}^{(i)} \quad (16)$$

where the last term is defined by:

$$\hat{S}_{i_p}^{(i)} = -\pi r^2 \sum_{l_p=1}^{n_p} \left( \int_{\Omega} m^i \eta_{i_p}(m, z) \int_0^{+\infty} \beta(z, m, m') \eta_{l_p}(m', z) dm' dm \right) \quad i_p = 1, \dots, n_p - 1 \quad (17)$$

$$\hat{S}_{n_p}^{(i)} = \pi r^2 \sum_{l_p=1}^{n_p} \left( \sum_{k_p=1}^{n_p} \frac{1}{2} \iint_{\Omega} (m + m')^i \beta(z, m, m') \eta_{l_p}(m, z) \eta_{k_p}(m', z) dm dm' \right. \\ \left. - \int_{\Omega} m^i \eta_{n_p}(m, z) \int_0^{+\infty} \beta(z, m, m') \eta_{l_p}(m', z) dm' dm \right) \quad (18)$$

240



with  $\bar{\Omega} = \{(m, m') > 0 | (m + m') \in \Omega\}$ . The set  $\bar{\Omega}$  represents the set of couples of particles which form, when aggregating, particles with mass in the interval  $\Omega$ .

Let us consider now the  $k$ -th section for the family  $i_p$ , defined by  $[m_{i_p, k-1}; m_{i_p, k}]$ . For  $i = 0$  and  $i = 1$ , Eq. (16) gives the equations governing the evolution of the number of particles and mass of particles of the family  $i_p$  in the  $k$ -th mass interval  
 245 for unit volume of the mixture, respectively:

$$\frac{d}{dz} (N_{i_p, k} w r^2) = -2r p w_{i_p}^{(0)} N_{i_p, k} + \hat{S}_{i_p, k}^{(0)} \quad (19)$$

$$\frac{d}{dz} (M_{i_p, k} w r^2) = -2r p w_{i_p}^{(1)} M_{i_p, k} + \hat{S}_{i_p, k}^{(1)} \quad (20)$$

We remark that so far we have written a general form of the moment equations, which are valid independently from the  
 250 particular approach used to solve them (QMOM or TSM). As previously stated, when the TSM method is adopted, the integral terms on the right-hand side of the two previous equations ( $w_{i_p}^{(\cdot)}$  and  $\hat{S}_{i_p, k}^{(\cdot)}$ ) are calculated first by reconstructing the continuous mass distributions in each section from the known moments (number and mass of ash particles in the  $k$ -th section per unit volume of the mixture), and then approximating the integrals with the Gauss-Legendre quadrature formulas.

We also observe that when the equations for the mass of particles are added together (summed over the particles families  
 255 and over the sections), the aggregation terms cancel out, and the following transport equation is obtained:

$$\frac{d}{dz} \left( \sum_{i_p=1}^{n_p} \sum_{k=1}^{n_s} M_{i_p, k} w r^2 \right) = -2r p \sum_{i_p=1}^{n_p} \sum_{k=1}^{n_s} w_{i_p, k}^{(1)} M_{i_p, k} \quad (21)$$

which gives the total mass of ash particles per unit volume of the mixture lost because of particle sedimentation from the plume.

The right-hand side of the previous expression can be used in the mass conservation equation for the volcanic mixture  
 260 accounting for atmosphere entrainment and particle sedimentation, which writes as:

$$\frac{d}{dz} (\rho_{mix} w r^2) = 2r \rho_{atm} U_\epsilon - 2r p \sum_{i_p=1}^{n_p} \sum_{k=1}^{n_s} w_{i_p, k}^{(1)} M_{i_p, k}, \quad (22)$$

where  $\rho_{atm}$  is the density of the atmosphere and  $U_\epsilon$  is the entrainment velocity defined as in Hewett et al. (1971):

$$U_\epsilon = \alpha_\epsilon |U_{sc} - U_{atm} \cos \phi| + \gamma_\epsilon |U_{atm} \sin \phi|.$$

In the previous equation,  $\alpha_\epsilon |U_{sc} - U_{atm} \cos \phi|$  is entrainment by radial inflow minus the amount swept tangentially along the  
 265 plume margin by the wind, and  $\gamma_\epsilon |U_{atm} \sin \phi|$  is entrainment from wind. Equation (22) states that the variation of mass flux along the plume axis (left-hand side term) is due to ingestion of atmospheric air into the column (first right-hand side term) and loss of particles from the column margins (second right-hand side term).

The horizontal and vertical components of the momentum balance are derived from Newton's second law and the variation of mass flux as:

$$270 \frac{d}{dz} (\rho_{mix} w r^2 u) = 2r U_\epsilon u_e \rho_{atm} - 2u p r \sum_{i_p=1}^{n_p} \sum_{k=1}^{n_s} w_{i_p, k}^{(1)} M_{i_p, k}, \quad (23)$$



$$\frac{d}{dz} (\rho_{mix} w r^2 v) = 2r U_\epsilon v_e \rho_{atm} - 2vpr \sum_{i_p=1}^{n_p} \sum_{k=1}^{n_s} w_{i_p,k}^{(1)} M_{i_p,k}, \quad (24)$$

and

$$\frac{d}{dz} (\rho_{mix} w^2 r^2) = gr^2 (\rho_{atm} - \rho_{mix}) - 2wpr \sum_{i_p=1}^{n_p} \sum_{k=1}^{n_s} w_{i_p,k}^{(1)} M_{i_p,k}. \quad (25)$$

On the horizontal directions (Eqs. 23 and 24), the momentum of the eruptive mixture varies due to the wind (first right-hand side term) and the loss of particles (second right-hand side term), while on the vertical axis (Eq. 25) the momentum is affected by the gravitational acceleration term and the fall-out of particles.

Mixture temperature  $T_{mix}$  varies when plume rises and in this version of PLUME-MoM temperature, in a manner similar to that described in Folch et al. (2016), is computed from the total specific energy of the mixture  $E$ , defined as the sum of mixture specific enthalpy, potential energy and kinetic energy as:

$$E = H + gz + \frac{1}{2} U_{sc}^2. \quad (26)$$

The specific enthalpy of the mixture  $H$  is written as the mass weighted average of the enthalpies of its components:

$$H = x_{da} C_{atm} T_{mix} + x_s C_s T_{mix} + x_{wv} (h_{wv0} + C_{wv} (T_{mix} - T_{ref})) + x_{lw} (h_{lw0} + C_{lw} (T_{mix} - T_{ref})) + x_i C_i T_{mix} + x_{vg} C_{vg} T_{mix}. \quad (27)$$

where the terms on the right-hand side express the contributions to mixture enthalpy of dry air, solid particles, water vapour, liquid water, ice and other volcanic gases, respectively. All the mass fractions are denoted with the notation  $x_{(\cdot)}$  and they refer to the mass fraction of the component  $(\cdot)$  with respect to the whole mixture. Similarly, the notation  $C_{(\cdot)}$  is used to represent the specific heat capacities of the different components. In Eq. (27),  $h_{wv0}$  and  $h_{lw0}$  are the enthalpies at a reference temperature ( $T_{ref} = 273.15$  K) per unit mass of water vapour and liquid water, respectively.

By denoting with  $w_{atm}$  the specific humidity of the atmosphere (mass of water vapour in a unit mass of moist air, expressed here as kilograms of vapour per kilogram of air), the following conservation equation for the total energy of the eruptive mixture can be written:

$$\frac{d}{dz} (\rho_{mix} w r^2 E) = 2\pi r U_\epsilon \rho_{atm} \left( C_{atm} T_{atm} (1 - w_{atm}) + w_{atm} (h_{wv0} - C_{wv} T_{atm}) + gz + \frac{1}{2} U_{atm}^2 \right) - 2pr \sum_{i_p=1}^{n_p} \sum_{k=1}^{n_s} \left( C_{s,i_p} T_{mix} + \frac{1}{2} U_{sc}^2 \right) w_{i_p,k}^{(1)} M_{i_p,k}. \quad (28)$$

On the right-hand side of Eq. (28) the terms responsible for the variation of mixture energy are listed. These terms include the interaction of the eruptive mixture with the atmosphere (which is assumed to contain water) and the loss of thermal and kinetic energy due to the sedimentation of solid particles.



295 The transport of dry air through the column is modelled as:

$$\frac{d}{dz} (\rho_{mix} x_{da} w r^2) = 2r \rho_{atm} U_{\epsilon} (1 - w_{atm}). \quad (29)$$

Eq. (29) states that the entrainment of dry air into the column is responsible for the variation of dry air mass flux. Analogously, the transport of water is affected by the ingestion into the the column of atmospheric water as:

$$\frac{d}{dz} (\rho_{mix} x_w w r^2) = 2r \rho_{atm} U_{\epsilon} w_{atm}, \quad (30)$$

300 where  $x_w$  is the mass fraction of water (which can be in either vapour, liquid and ice form) in the mixture.

Finally, PLUME-MoM-TSM accounts for the presence of additional volcanic gases:

$$\frac{d}{dz} \left( \sum_k \rho_{mix} x_k w r^2 \right) = 0. \quad (31)$$

From Eq. (31) we see that the volcanic gases mass flux is assumed to be constant along the plume. We are thus assuming that all volcanic gases reach the top of the plume (or the neutral buoyancy level) where they are released into the atmosphere.

305 The system of Eqs. (19-31), describing the steady dynamics of volcanic plume rise in the atmosphere, is solved numerically by PLUME-MoM-TSM. A 4-5th order Dormand-Prince Runge-Kutta method (Dormand and Prince, 1980), which automatically adapt the integration step to control the numerical error, is implemented in a Fortran 90 code for the numerical integration of the system of ordinary differential equations. The computational time requested for a run is of the order of a few tenths of seconds for a simulation without aggregation, and slightly longer for simulations modeling also the aggregation process.

### 310 2.3 Phase changes of water

The present version of PLUME-MoM accounts for phase change of water as a function of the pressure and temperature conditions. Water (in vapour, liquid or ice phase) in the mixture can be either magmatic, added at the vent as liquid, or incorporated through ingestion of moist atmospheric air. Within the eruptive column, phase changes lead the water to be partitioned into vapour, liquid and ice:

$$315 \quad x_w = x_{wv} + x_{lw} + x_i, \quad (32)$$

where  $x_w$  is the water mass fraction in the eruptive mixture, while  $x_{wv}$ ,  $x_{lw}$  and  $x_i$  are the mass fractions of water vapour, liquid water and ice phases, respectively.



In the following, we will use the subscript  $da$ ,  $wv$  and  $vg$  to refer to dry air, water vapour and volcanic gases, respectively. With this notation, assuming that the mixture of dry air, water vapour and volcanic gases behaves as an ideal gas, we can write the following relationships between atmospheric pressure  $P_{atm}$ , phases partial pressures  $P_{(\cdot)}$  and molar fractions  $n_{(\cdot)}$ :

$$\begin{aligned} P_{atm} &= P_{da} + P_{wv} + P_{vg}, \\ P_{da} &= n_{da} P_{atm}, \\ P_{wv} &= n_{wv} P_{atm}, \\ P_{vg} &= n_{vg} P_{atm}. \end{aligned} \quad (33)$$

Molar fractions of water vapour ( $n_{wv}$ ), volcanic gases ( $n_{vg}$ ) and dry air ( $n_{da}$ ) in the gas phase of the volcanic mixture (for which it holds  $n_{wv} + n_{da} + n_{vg} = 1$ ) are given by:

$$n_{wv} = \frac{\frac{x_{wv}}{mw_{wv}}}{\frac{x_{wv}}{mw_{wv}} + \frac{x_{vg}}{mw_{vg}} + \frac{x_{da}}{mw_{da}}}, \quad (34)$$

$$n_{vg} = \frac{\frac{x_{vg}}{mw_{vg}}}{\frac{x_{wv}}{mw_{wv}} + \frac{x_{vg}}{mw_{vg}} + \frac{x_{da}}{mw_{da}}}, \quad (35)$$

$$n_{da} = \frac{\frac{x_{da}}{mw_{da}}}{\frac{x_{wv}}{mw_{wv}} + \frac{x_{vg}}{mw_{vg}} + \frac{x_{da}}{mw_{da}}}, \quad (36)$$

where  $mw_{wv} = 0.018 \text{ kg mole}^{-1}$  and  $mw_{da} = 0.029 \text{ kg mole}^{-1}$  are the molar weights of water vapour and dry air. The molar weight of the additional mixture of volcanic gases  $mw_{vg}$  is:

$$mw_{vg} = \frac{\sum_k x_k}{\sum_k \frac{x_k}{mw_k}}, \quad (37)$$

where  $x_k$  and  $mw_k$  are the mass fraction with respect to the mixture and the molar weight of the  $k$ -th volcanic gas. For  $\text{CO}_2$  and  $\text{SO}_2$  (most abundant volcanic gases after water),  $mw_k$  are  $0.044 \text{ kg mole}^{-1}$  and  $0.064 \text{ kg mole}^{-1}$  respectively.

Once the conservation equation for the total energy (Eq. 28) is integrated, giving a new value of the total specific energy  $E$ , the specific enthalpy of the eruptive mixture  $H$  is computed from Eq. (26). Then, mixture temperature ( $T_{mix}$ ) and water mass fractions ( $x_{wv}$ ,  $x_{lw}$ ,  $x_i$ ) are computed from the known value of  $H$  by finding the values which satisfy Eq. (27) and Eqs. (32-36).

### 2.3.1 Addition of external liquid water

The addition of external liquid water to the volcanic mixture is one of the new features of PLUME-MoM-TSM. As in Koyaguchi and Woods (1996), we assume that magma-water mixing takes place at the vent location and that the thermal equilibrium between the eruptive mixture and the external water is reached before the interaction of the mixture with the atmosphere.



340 Before addition of external water, specific enthalpy at the vent is:

$$H_{vent} = x_s C_s T_{mix0} + x_{wv} [h_{wv0} + C_{wv} (T_{mix0} - T_{ref})] + x_{vg} C_{vg} T_{mix0}, \quad (38)$$

where  $x_s$  and  $x_{wv}$  are the mass fractions of particles and magmatic water vapour in the erupted magma and  $T_{mix0}$  is its temperature.

345 If external liquid water is added at the vent, the eruptive mixture formed by magma and liquid water is initialized by computing a new enthalpy ( $H_{vent_{new}}$ ):

$$H_{vent_{new}} = x_{erupt} H_{vent} + x_{lw_{ext}} [h_{lw0} + C_{lw} (T_{lw_{ext}} - T_{ref})], \quad (39)$$

where  $x_{lw_{ext}}$  is the mass fraction of external liquid water at temperature  $T_{lw_{ext}}$ , and  $x_{erupt} = 1 - x_{lw_{ext}}$  is the magmatic mass fraction. From the value of  $H_{vent_{new}}$ , we update magma temperature and water partitions by following the procedure described in Appendix A.

350 To test the consistency of the results produced by PLUME-MoM-TSM in the presence of external water, in the Supplementary Materials we reproduced some of the figures presented by Koyaguchi and Woods (1996).

## 2.4 Umbrella spreading model

As previously stated, PLUME-MoM-TSM includes the possibility to simulate the initial spreading of the umbrella cloud associated with a volcanic column. When this option is activated, the column equations are solved up to the neutral buoyancy  
355 level, where the density of the mixture equals that of the atmosphere. Above this height, the initial transport of the ash is dominated by a radial spreading, due to the fact that the plume still has a vertical momentum, which produce an overshoot in the atmosphere and then an intrusion at the neutral buoyancy level as a gravity current. This dynamics is described by a different set of equations from those of the column, and here we use a system of “shallow-water” equations similar to that developed by Baines (2013); Johnson et al. (2015).

360 The intruding fluid is assumed to spread horizontally at the neutral buoyancy level as a shallow layer (with respect to the atmosphere thickness) so that the vertical accelerations are negligible and the pressure distribution within the umbrella is hydrostatic. In addition, we assume that, due to turbulent mixing, the density of fluid is uniform within the umbrella, and this implies that variations in the thickness of the layer generate horizontal pressure gradients driving the motion, which is resisted by turbulent drag. Furthermore, for the umbrella cloud model, we neglect the loss of particles from its base, and thus the density  
365 can be considered constant. Differently from the model of Johnson et al. (2015), where the volumetric flux intruding from the column into the atmosphere is provided by imposing a radial axisymmetric flux at a prescribed distance from the plume centerline (with fixed initial thickness), here the flux is provided, in both mass and momentum equations, through appropriate source terms derived from the neutral buoyancy level horizontal section of the column. In this way, it is possible to consider also the initial horizontal velocity of the umbrella cloud resulting from the horizontal momentum of the volcanic plume.



370 With these assumptions, if we denote with  $h$  the umbrella cloud thickness and with  $(u, v)$  the horizontal components of the velocity, the equations for the conservation of volume and horizontal momentum write as:

$$\begin{cases} \frac{\partial h}{\partial t} + \frac{\partial}{\partial x}(hu) + \frac{\partial}{\partial y}(hv) = \tilde{w} \\ \frac{\partial}{\partial t}(hu) + \frac{\partial}{\partial x}\left(hu^2 + \frac{N^2 h^3}{12}\right) + \frac{\partial}{\partial y}(huv) = -C_D(u - u_a)|\mathbf{u} - \mathbf{u}_a| + [u_{nbl} + \gamma_x(x, y)w_{nbl}]\tilde{w} \\ \frac{\partial}{\partial t}(hv) + \frac{\partial}{\partial x}(huv) + \frac{\partial}{\partial y}\left(hv^2 + \frac{N^2 h^3}{12}\right) = -C_D(v - v_a)|\mathbf{u} - \mathbf{u}_a| + [v_{nbl} + \gamma_y(x, y)w_{nbl}]\tilde{w} \end{cases} \quad (40)$$

On the left-hand sides of the momentum equations,  $N$  is the Brunt-Väisälä frequency, which represents an upper limit for the frequency of internal gravity waves in the atmosphere. Its value is computed at the neutral buoyancy level from the atmospheric density profile as follows:

$$N = \sqrt{-\frac{g}{\rho_{nbl}} \frac{\partial \rho_{atm}}{\partial z}}.$$

On the right-hand side of all the equations in system (40),  $\tilde{w}$  is the volumetric flux source derived from the vertical velocity at the vent:

$$\tilde{w} = w_{nbl} \cdot \chi_{|(x^2+y^2 < r_{nbl})} \quad (41)$$

380 and  $\gamma_x$  and  $\gamma_y$  are two functions which take into account the vertical gradient of the plume radius at the neutral buoyancy level:

$$\begin{cases} \gamma_x(x, y) = \frac{x}{r_{nbl}} \cdot \frac{dr}{dz} \cdot \chi_{|(x^2+y^2 < r_{nbl})} \\ \gamma_y(x, y) = \frac{y}{r_{nbl}} \cdot \frac{dr}{dz} \cdot \chi_{|(x^2+y^2 < r_{nbl})} \end{cases} \quad (42)$$

In this way, the volume and the momentum flux derived from the plume model are correctly passed to the umbrella model.

385 The system of partial differential equations is solved with a transient finite-volume code based on the numerical solver presented in de' Michieli Vitturi et al. (2019), where an implicit-explicit Runge-Kutta scheme (Ascher et al., 1997) is adopted to compute explicitly the flux terms on the left-hand side of the equations and the source terms, and implicitly the drag terms in the momentum equations. The integration time step is constrained by a CFL condition and the solution is advanced in time until a steady upwind spreading is reached. An example of the output of the coupled plume-umbrella models is presented in Fig. 4.

### 390 3 Applications

In this section we present a suite of simulations to highlight the novelties introduced in this version of PlumeMoM and to constrain model parameters. First, we model the spreading of the umbrella cloud for the eruption of Calbuco volcano in southern Chile in April 2015, by comparing simulation results with rates of umbrella cloud expansion derived from satellite observations. This allows us to constrain the coefficient  $C_D$  in Eq. (40), controlling the spreading of the umbrella. Then, by

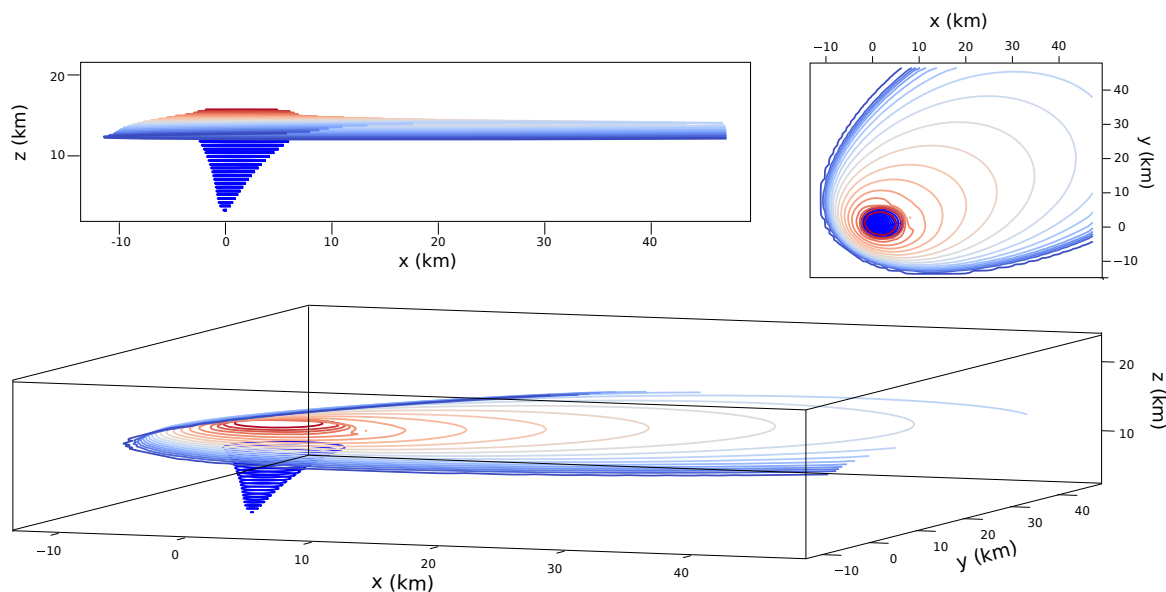


**Figure 4.** Lateral, top and oblique views of the plume and the umbrella. The 3-D coordinate system (x,y,z) is centered horizontally at the plume base location, and vertically at the sea level. Up the neutral buoyancy level the plume horizontal sections are calculated by the steady state model. Above the neutral buoyancy level, the colored contours represent thickness levels of the steady solution computed by the transient umbrella model.

395 using a modified standard atmosphere, an analysis of the effects of wind, atmospheric humidity, and mass flow rate on the  
upwind spreading of the umbrella cloud is presented.

### 3.1 April 2015 Calbuco eruption

We present here model results obtained for the two phases of the eruption of Calbuco volcano in April 2015 (Romero et al.,  
2016; Castruccio et al., 2016; Van Eaton et al., 2016). Calbuco is one of the most active volcanoes of the southern Chilean  
400 Andes and on the evening of 22 April 2015, for the first time in 43 years, Calbuco erupted, producing a sub-plinian column with  
maximum plume heights exceeding 15 km above the vent (Pardini et al., 2018). Preceded by an hour-long period of volcano-  
tectonic events, the first phase started at 21:04 UTC and lasted approximately 1.5 hours producing tephra dispersed mostly in  
north and northeast directions and causing a 20-km exclusion zone to be declared. After a 5.5 hours break, at 03:54 UTC on 23  
April 2015, a second larger explosive phase began. This second phase lasted approximately 6 hours, with a drop in activity of  
405 1 hour approximately 2 hours after its onset (Van Eaton et al., 2016). After the second phase, discrete small explosions caused  
further ash emission up to 2 km height, with a major pulse which resulted in a 4 km high column on 30 April (Romero et al.,  
2016). Ash from the different phases of the eruption reached Brasil, Chile, Argentina and Uruguay, causing the canceling of  
international flights in and out of several major cities in South America.



Following Reckziegel et al. (2019), the total grain size distribution released at the vent for both the phases has been initialized  
410 with of a bi-modal distribution with 11 particle classes from  $-1\phi$  to  $9\phi$ , with densities increasing linearly with  $\phi$  from 2300  
to  $2700 \text{ kg m}^{-3}$ . Particle sphericity, mostly affecting the loss of particles through the terminal velocity equation (Textor et al.,  
2006b), has been fixed to 0.8. Following Van Eaton et al. (2016), we assumed 5 wt% of magmatic water, plus an additional  
5 wt% of cooler surface water, possibly associated with the presence of a summit glacier prior to the eruption. The initial  
temperature of the magmatic mixture has been fixed to 1173 K and, after the mixing with the external water, a temperature of  
415 1006 K has been found for the base of the plume. The initial plume velocity for both the phases has been fixed to  $250 \text{ m s}^{-1}$ ,  
and the radius has been changed for the two phases in order to match the height of the intrusion of the umbrella cloud in the  
atmosphere and its main spreading direction. This results in a mass eruption rate of  $9.54 \times 10^6 \text{ kg s}^{-1}$  for the first phase and  
 $2.02 \times 10^7 \text{ kg s}^{-1}$  for the second one. Varying the initial velocity, while keeping fixed the height of the neutral buoyancy level,  
produced very similar results in terms of mass eruption rates.

420 In Fig. 5 some of the plume model outputs obtained for the first phase are reported. In each panel, values below the neutral  
buoyancy level are plotted with a solid line, while dashed lines represent model results above it. Plume velocity (top-left panel)  
initially decelerates very rapidly in the gas thrust region, and then decelerates more gently and almost linearly with height,  
up to the neutral buoyancy level. Mixture density, because of the large amount of air entrained from the column margin and  
heated in the gas thrust region, rapidly decreases below atmospheric density making the plume positively buoyant (see the  
425 plot of the relative density in the top-right panel). The water vapour initially present in the rising mixture, with the additional  
contribution of the moist entrained in the plume, stays in the gaseous state up to a height above sea level of approximately 8.5  
km, above which ice starts to form. At the neutral buoyancy level, almost all the water present in the plume is constituted by  
ice (middle-left panel). Particles are lost during the rise, but the fraction of the initial amount lost up to the neutral buoyancy  
level is relatively small, ranging from a maximum of 0.24 for  $\phi = -1$  to fractions smaller than 0.01 for  $\phi \geq 3$ . This means that  
430 almost all the particles erupted reach the neutral buoyancy level, and that the initial grain size distribution differs very little  
from that feeding the umbrella cloud (bottom-left panel). In any case, almost immediately above the vent, due to the large  
entrainment, the mass of particles, as that of water, become rapidly a small fraction of the total mass of the mixture, with the  
dry air being the more abundant phase (middle-right panel). At the neutral buoyancy level, reached at 12.7 km above sea level,  
the plume radius is 3935 m (see bottom-right panel) and the mass flow rate injected in the umbrella cloud is  $6.64 \times 10^8 \text{ kg s}^{-1}$   
435 (corresponding to a volume flow rate of  $2.21 \times 10^9 \text{ m}^3 \text{ s}^{-1}$ ). The bottom-right panel presents a 3D view of the plume, showing  
the weak bending of the plume axis due to both the moderate wind and the magnitude of the eruption.

The simulation performed for the second phase produced similar results, and the main output variables are plotted in Fig.  
6. For this simulation, the height of the neutral buoyancy level increased to approximately 13.6 km, at which the plume radius  
is 3814 m, with a mass flow rate injected in the umbrella cloud of  $8.38 \times 10^8 \text{ kg s}^{-1}$  (corresponding to a volume flow rate of  
440  $3.22 \times 10^9 \text{ m}^3 \text{ s}^{-1}$ ).

For both the phases, the outputs at the neutral buoyancy level of the plume module of PLUME-MoM-TSM (volumetric  
flow rate, radius and horizontal velocities) were used as input of the umbrella cloud module. For this application, we varied  
the drag coefficient  $C_D$  of the umbrella cloud model in order to find the value which better reproduced the spreading in the

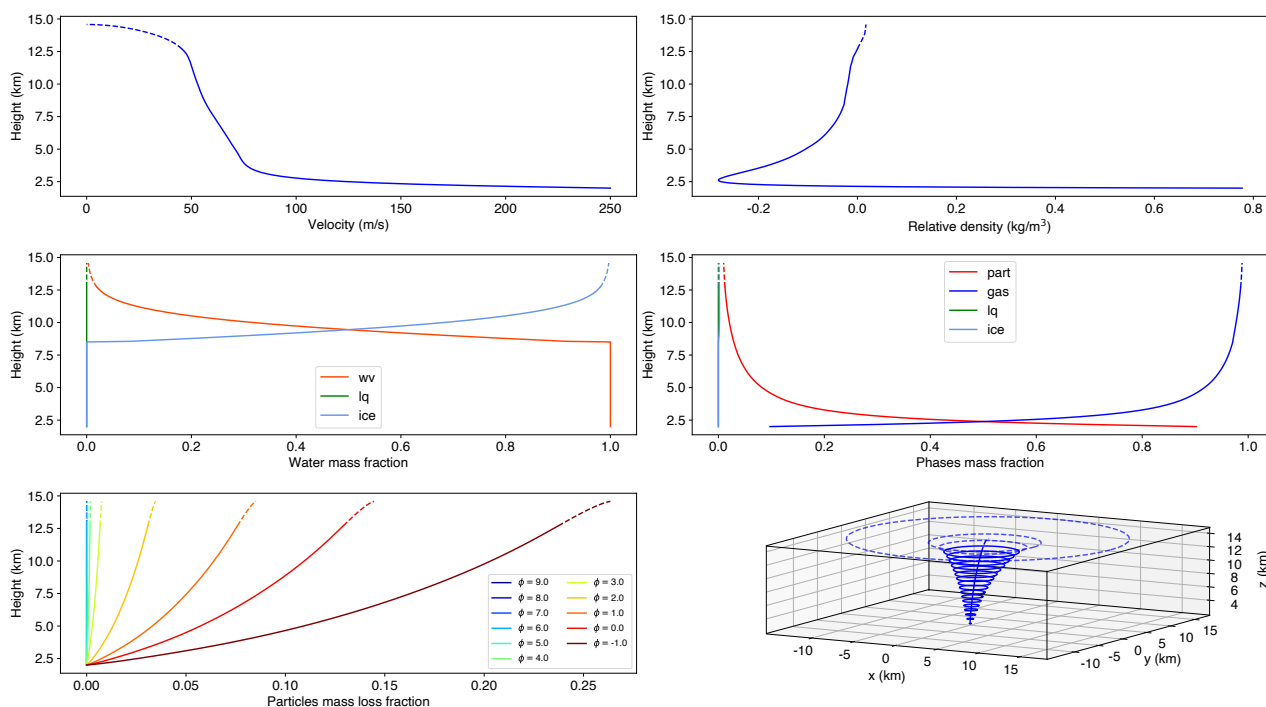


**Figure 5.** Plume model results for the first phase of the April 2015 Calbuco: velocity profile (top left); relative density, defined as the difference between the density of the volcanic mixture and the density of the surrounding air (top right); relative mass fractions of water phases (middle left); mass fractions of particles, gas (water and dry air), liquid water and ice (middle right); relative mass fractions (with respect to the initial amount) of particles lost during the rise for the different bins (bottom left); three dimensional view of the plume. Height reported on the left axis of the 2D plots are measured above sea level. Please note that values up to the neutral buoyancy level are plotted with solid lines, while those corresponding to model solutions above the neutral buoyancy level are plotted with dashed lines.

atmosphere observed during the eruption. Three values were tested (0.5, 1 and 2) by carrying on the simulations for 1.5 hour  
 445 and 2 hours for the first and second phase, respectively. At each time step we computed: (i) the upwind spreading, defined here as the maximum horizontal distance from the vent in the opposite direction to that of the wind at the neutral buoyancy level; (ii) the radius of a circle with area equivalent to that of the modeled umbrella cloud. These values are plotted, at intervals of 300 s, in the left panels of Fig. 7, with red lines for the upwind distances and blue lines for the equivalent radius. First of  
 450 all, we can see from the plots that for all values of  $C_D$  a steady upwind distance is reached at the end of the simulation, and that by changing (increasing or decreasing) the drag coefficient of a factor 2 with respect to the value  $C_D = 1$ , the upwind spreading changes approximately of 10%. The blue lines in the left panels of Fig. 7 are compared with the series of values for the umbrella radius reported in Van Eaton et al. (2016), obtained detecting the edge of the umbrella from GOES-13 satellite images and here plotted with blue markers. From the results plotted in the figure, we can see that the values obtained with

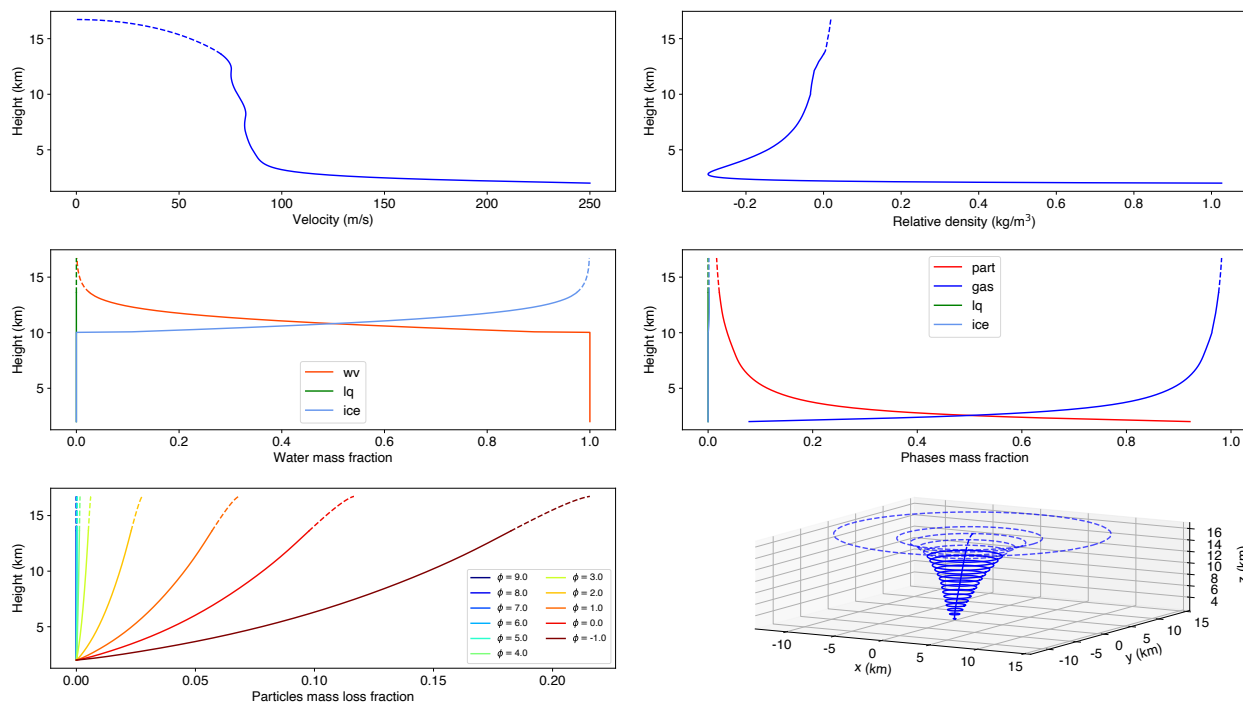


**Figure 6.** Plume model results for the second phase of the April 2015 Calbuco: velocity profile (top left); relative density, defined as the difference between the density of the volcanic mixture and the density of the surrounding air (top right); relative mass fractions of water phases (middle left); mass fractions of particles, gas (water and dry air), liquid water and ice (middle right); relative mass fractions (with respect to the initial amount) of particles lost during the rise for the different bins (bottom left); three dimensional view of the plume. Height reported on the left axis of the 2D plots are measured above sea level. Please note that values up to the neutral buoyancy level are plotted with solid lines, while those corresponding to model solutions above the neutral buoyancy level are plotted with dashed lines.

455  $C_D = 1$  seems to better match the observation, with a small overestimate at the beginning and a small underestimate at the end of the simulation. For this reason, in the following of the paper, we used this value as reference value.

460 In the right panels of Fig. 7 the contours of umbrella thickness at the end of the simulations are plotted, with different lines for the different values of  $C_D$ . The larger volumetric flow rate injected at the neutral buoyancy level for the second phase resulted in a thicker cloud, with a total height of column and umbrella of approximately 15.5 km and 17.5 km above sea level for the first and second phase, respectively. These values compare well with those reported in Van Eaton et al. (2016). Also from these panels we can observe the expected larger spreading of the umbrella cloud for smaller values of  $C_D$ . These results highlight the fact that intrusive gravity current dominates in the initial stages of the dispersion of ash at the neutral buoyancy level and large upwind and crosswind spreadings of the umbrella cloud with respect to the vent location (denoted with a red

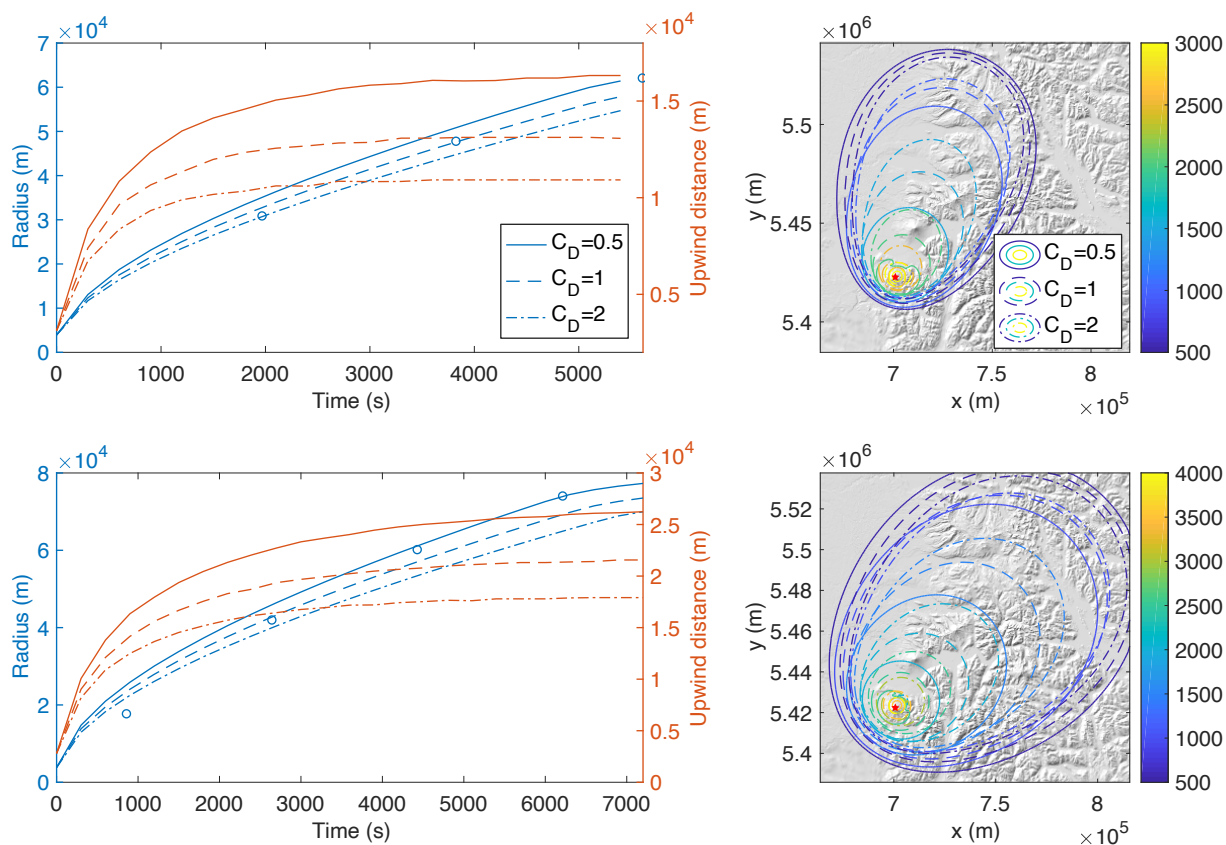


**Figure 7.** Umbrella cloud spreading for the two initial phases of the April 2015 Calbuco eruption. The top panels refer to the first phase, while the bottom panels to the second phase. On the left plot are plotted the umbrella equivalent radius and the upwind distance versus time; on the right panels the contours of thickness at the end of the simulations are shown. In all the panels, different lines (solid, dashed and dash-dotted) represent the three different values of  $C_D$  used in this work.

star in the right panels of Fig. 7) are produced also for subplinian eruptions. For the simulation presented in this work, almost 90% of the maximum upwind spreading is reached in 30 minutes after the onset of the intrusion at the neutral buoyancy level.

465 In the analysis presented so far, we have not accounted for the effect of aggregation. To better understand if aggregation could affect the spreading of the umbrella for this scenario, we repeated the plume rise simulation for the first phase of the April 2015 Calbuco eruption by enabling aggregation between particles and analyzing the changes in the height of the neutral buoyancy level and the grain size distribution of particles still present in the plume and released from its margin at that height. For this set of simulations, two coarser bins with an initial negligible amount of particles have been added to the total grain size  
 470 distribution. This allow for the formation of aggregates larger than the particles present in the original size spectrum. Density of the aggregates has been fixed to  $1500 \text{ kg m}^{-3}$ , resulting in lower settling velocity than the original particles, the size begin equal.

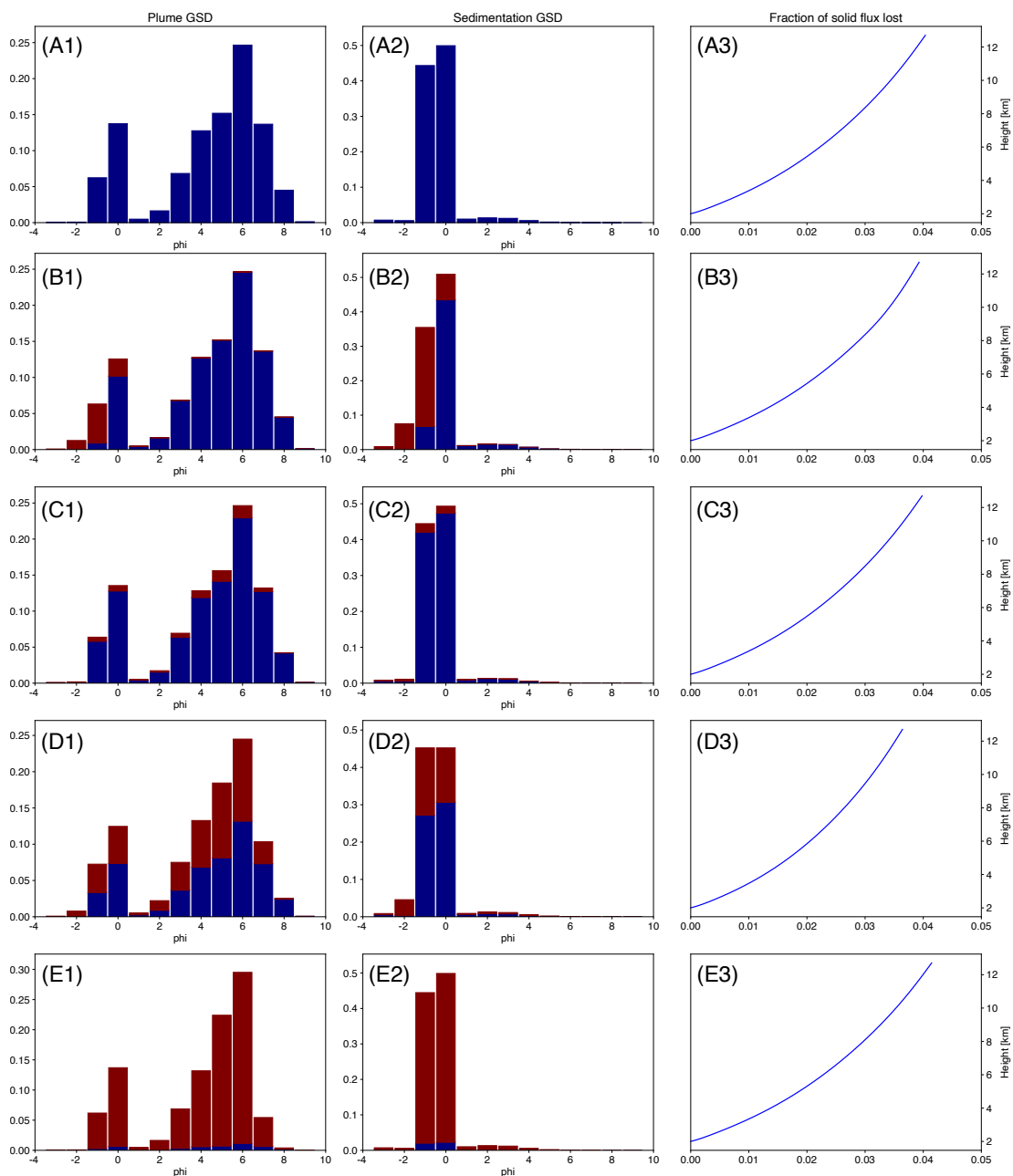


**Figure 8.** Grain size distribution at the neutral buoyancy level: within the plume (left panels) and released from the plume margins (right panels). The blue bars represent the amount of the particles released at the vent, while the maroon bars represent the amount of aggregates. The results of the simulation without aggregation are plotted in panels A1 and A2. The results obtained with the wet aggregation model presented in Costa et al. (2010) are plotted in panels B1 and B2. The results obtained with a constant aggregation kernel and values of  $10^{-15}$ ,  $10^{-14}$  and  $10^{-13}$  are plotted in panels C, D and E, respectively.



The results of the simulation without aggregation are plotted in the top panels of Fig. 8. The grain size distribution within the plume at the NBL is plotted in panel A1 of Fig. 8, the grain size distribution of the particles lost from the plume margins at the same height is plotted in panel A2, and the fraction of the initial total solid flux lost with height (which indicates the amount of particles lost from the plume edges during the rise) is shown in panel A3. The grain size distribution at the neutral buoyancy level does not differ significantly from that at the vent, and this is due to the fact that the amount of particles lost during the rise is very small (approx 4%).

As a first aggregation test, we used a modified version of the wet aggregation kernel introduced in Costa et al. (2010), defined as the product of a collision frequency function and a sticking efficiency function (see Appendix A3). According to this model, to aggregate, a collision must occur between the particles and when that collision occurs the particles must adhere to one another. Collisions between particles are associated to different mechanism, as Brownian motion, laminar and turbulent fluid shear and differential settling velocity. Following Costa et al. (2010), all these contribution are considered in the calculation of the collision frequency function. In our formulation, the sticking efficiency depends on the amount of liquid water and ice present in volcanic plume. For the simulations of the Calbuco eruption, as shown in Fig. 5, only ice forms above an height of 8 km asl. For this reason, aggregation is quite limited and the grain size distributions of the particles within the plume and the particles released from the plume margin at the NBL show very small differences with the simulation without aggregation, and it is limited to the coarser particles. This is mostly due to the fact that the dominant collisional mechanism is the differential settling velocity, which is larger for coarser particles. It is important to note that the neutral buoyancy level differs from that obtained without aggregation by less than 0.1%, and also the total amount of particles lost from the plume does not differ significantly.

In order to better understand the effect of aggregation, we performed additional simulations with a constant kernel, starting from a value  $\beta = 10^{-15} \text{ m}^3\text{s}^{-1}$ , up to a value  $\beta = 10^{-13} \text{ m}^3\text{s}^{-1}$ . The simulation with  $\beta = 10^{-15} \text{ m}^3\text{s}^{-1}$  shows small differences with that without aggregation, with small amounts of aggregated particles produced (represented in panel B1 of Fig. 8 with the red bars). Because of the adoption of a constant kernel, aggregates form in each bin of the initial grain size distribution. By increasing  $\beta$  of an order of magnitude to a value of  $10^{-14} \text{ m}^3\text{s}^{-1}$ , the amount of aggregates become significant (more than 50% for some bins), and also the relative amounts of particles released from the plume margins at the neutral buoyancy level differs from those obtained without aggregation. Despite that, we observe that the height of the neutral buoyancy level of the plume does not change, and also the overall bi-modal shape of the total (aggregated and non-aggregated particles) distribution does not change substantially. This is because, with the binary aggregation and the constant aggregation kernel considered here, most of the aggregation occurs "intra-bin", i.e. produce an aggregate with a volume, or mass, which belongs to the same bin of particles forming the new aggregate. In fact, for bin sizes of 1 phi, and a uniform mass distribution within each bin, the number of smallest particles within a bin is almost one order of magnitude smaller than the number of largest particles. Thus, with a constant kernel, aggregation of the smallest particles occurs much frequently, and the aggregate produced from a binary aggregation of these particles produce a new particle with an equivalent diameter (diameter calculated from the mass) still belonging to the same bin. In order to produce a larger change in the particle size distribution in the plume at the neutral buoyancy level, we have to increase the constant kernel to  $\beta = 10^{-13} \text{ m}^3\text{s}^{-1}$ , for which the fraction of aggregates is close to



97% of the total mass of particles in the plume (Fig. 8, panels E1 and E2). It is interesting to observe that even with such a large amount of aggregates, the total amount of particles lost during the rise does not change with respect to the simulation without aggregation, and also the height of the neutral buoyancy level differs from that obtained without aggregation only by 1 m. This result allows us to disregard aggregation for the sensitivity analysis presented in the next section, where the main outputs of the plume module used to initialize the umbrella spreading module are the volumetric flow rate and the height of the gas/particles mixture injected by the plume into the atmosphere at the neutral buoyancy level.

### 3.2 Umbrella cloud upwind spreading

In this section we present a sensitivity analysis of the upwind spreading of the umbrella cloud with respect to mass flow rate and to some parameters characterizing the meteorological profile above the vent. This study builds on the ideas of Carey and Sparks (1986), where the ratio of upwind spreading to the amount of axial displacement at the neutral buoyancy level was analyzed, with results based on theoretical and empirical information on column behaviour. The simulations presented here employ pressure, temperature and density atmospheric profiles modified from the International Standard Atmosphere (ISA) model. This model provides a common reference for temperature and pressure at various altitudes, and it is based on the subdivision of the atmosphere in layers where the absolute temperature  $T_{atm}$  against geopotential altitude  $h$  is assumed to vary linearly. Geopotential and orthometric heights differ little for low terrestrial atmosphere (Daidzic, 2019), and for this reason we can assume a linear dependence of temperature also against orthometric height. In the following, as common in meteorology, we refer to the negative of the rate of temperature change with altitude with the term "lapse rate", and we use for it the notation  $\Gamma$ . Once the bottom values and the lapse rate are known in an atmospheric layer, pressure, temperature and density profiles within the layer can be calculated by solving simultaneously the equation for vertical pressure gradient resulting from hydrostatic balance, the equation for temperature and the ideal gas law:

$$\begin{cases} \frac{\partial P_{atm}}{\partial z} = -\rho_{atm}(z)g \\ \frac{\partial T_{atm}}{\partial z} = -\Gamma_{atm} \\ \rho_{atm} = \frac{P_{atm}}{RT_{atm}} \end{cases} \quad (43)$$

When the option for a modified standard atmosphere is selected in PLUME-MoM-TSM, the first two equations are added to the set of ordinary differential equations solved numerically by the model, and the last one is employed to calculate explicitly the right-hand term of the first equation.

ISA lapse rates do not account for humidity effects and air is assumed to be dry. For this reason, when humidity is considered, appropriate corrections to the atmospheric profiles given by the ISA model need to be introduced. Moist unsaturated air cools with height at a slightly lower rate than dry air (Dutton, 2002) and in this work we adopt the following lapse rate correction to account for the presence of water vapour, as proposed in Daidzic (2019):

$$\Gamma_{atm} = \Gamma_d(1 - 0.856w_{atm}), \quad (44)$$

where  $\Gamma_{atm}$  and  $\Gamma_d$  are the moist and dry atmospheric lapse rates, respectively. According to Ahrens (2012), the average specific humidity in the lower troposphere ranges from  $0.004 \text{ kg kg}^{-1}$  at 60 degrees (north or south) to  $0.018 \text{ kg kg}^{-1}$  at



the equator, and its value exponentially decrease to values lower than  $10^{-5}$  kg kg<sup>-1</sup> above the tropopause. It follows that the  
540 sensitivity of lapse rates to the specific humidity value is minimal in the lower troposphere, and negligible above it.

Density of moist atmosphere also varies with water content, and the relationship between dry and moist air densities can be written as:

$$\rho_{atm} = \frac{\rho_d}{1 + \left(\frac{R_{wv}}{R_{air}} - 1\right) w_{atm}}, \quad (45)$$

where  $R_{wv}$  and  $R_{air}$  are the gas constant of water vapour and air, respectively.

545 With these equations, ISA lapse rates  $\Gamma_d$  and density  $\rho_d$  are corrected for the presence of humidity and it is possible to solve the system of Eqs. (43) for the modified pressure and temperature profiles. The specific humidity profile used in the simulations presented here has been derived from the data presented in Anderson et al. (1986), providing the values at the boundaries between the atmospheric layers, while the troposphere bottom value has been varied in the range 0.004-0.018 kg kg<sup>-1</sup>. Inside each layer, the logarithm of specific humidity is assumed to vary linearly.

550 In this work we also assume the wind speed being a continuous function of height which varies linearly in several layers. Observation indicate that on average wind speed profile has local minima at altitudes of about 20 km and about 90 km, where air masses are relatively stationary, and local maxima at altitudes of about 11 km and 70 km (Modica et al., 2007; Brasfield, 1954). While a quite wide range of values is observed for the first maximum at the tropopause, the value of the wind speed at 70 km varies less, and a speed of 65 m s<sup>-1</sup> is assumed in this work. For the wind speed minimum at 20 km altitude, we fix a  
555 value of 10 m s<sup>-1</sup>. With these assumptions, the relevant atmospheric profiles obtained for a moist atmosphere and with a wind speed of 20 m s<sup>-1</sup> at 11 km are plotted in Fig. 9, where the red markers in the last two panels denote the values we varied for the sensitivity analysis.

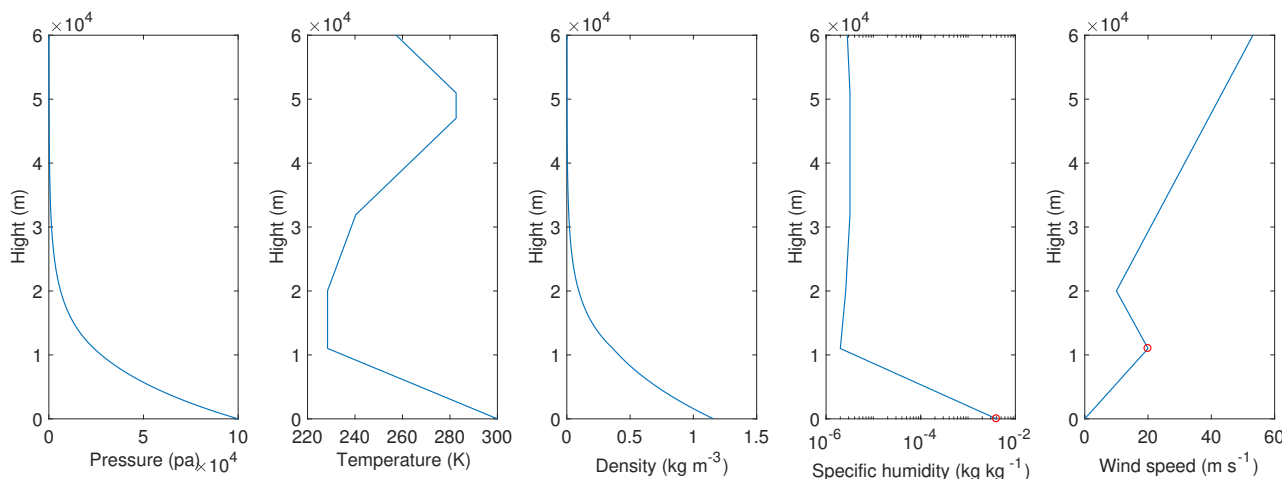


**Figure 9.** Atmospheric profiles for a dry atmosphere and with a  $20 \text{ m s}^{-1}$  wind speed at the tropopause (11 km asl). The red markers denote the values that can be changed in the modified standard atmosphere adopted in the model. The first three profiles (pressure, temperature and density) also change when the specific humidity at the sea level is changed.

Maximum upwind spreading of the umbrella cloud with respect to vent location represents an important information that coupled plume and umbrella models, or fully three-dimensional models (Cerminara et al., 2015; Suzuki and Koyaguchi, 2009) can provide. It has been noted that using only the output of integral plume models as source of VATD models generally underestimate the upwind depositions patterns of volcanic ash, and corrections accounting for the initial spreading of the umbrella as a gravity current result in a better agreement of ash distribution close to the eruptive source (Costa et al., 2013; Webster et al., 2020).

Most of the work done so far to couple the spreading of the umbrella cloud with advection-diffusion-sedimentation models focused on large events as the 1991 Pinatubo eruption, with a mass flow rate of the order of  $10^9 \text{ kg s}^{-1}$ . Less work has been devoted to smaller scenarios and for this reason here we focus on lower values of mass flow rate, in order to gain a better understanding of the relationship between mass flow rate, wind speed and upwind spreading. It is well known that upwind spreading increases with increasing mass flow rate and decreasing wind, but a quantitative relationship between them is unknown. Here, we varied three input parameters of the model: 1) the decadic logarithm of mass flow rate in the range 6 – 8 (i.e.  $\dot{m} = 10^6 - 10^8 \text{ kg s}^{-1}$ ); 2) the wind speed at the tropopause in the range 35 – 80  $\text{m s}^{-1}$ ; 3) the specific humidity at the sea level in the range 0.004-0.018  $\text{kg kg}^{-1}$ . A uniform probability has been assigned to all the input variables and the space of parameters has been sampled with a Latin Hypercube Sampling generating 700 elements. The other main input parameters used for this analysis are listed in Table 1. As previously stated, aggregation is disregarded here, because the effect on the input parameters of the umbrella module is negligible. In addition, as shown in de' Michieli Vitturi et al. (2015), also the initial total grain size distribution has a minimal control on plume height, and consequently on upwind umbrella spreading. For this reason, it has been kept fixed for all the simulations.



Input parameter	Symbol	Value
Vent height (asl)	$h_0$	1500 m
Initial water mass fraction	$x_w$	0.01
Initial temperature	$T_{mix0}$	1273 K
Initial velocity	$w_0$	$135 \text{ m s}^{-1}$

**Table 1.** Relevant input parameters of the plume model fixed for all the simulations of the sensitivity analysis.

For each simulation, the horizontal upwind distance from the vent of the umbrella cloud has been calculated from the output of umbrella spreading module (when a steady value is reached), and correlation plots with the three input parameters are presented in the first three panels of Fig. 10, where each red dot represents a different simulation. In general, we observe increasing upwind spreading with increasing mass eruption rate and decreasing wind speed at the tropopause, while the relative humidity does not seem to affect it. For a fixed value of the input parameters on the x-axis, the vertical spreading of the red dot cloud is associated with variations in the other input parameters. Each black line represents the average of the upwind spreading values at a given input value.

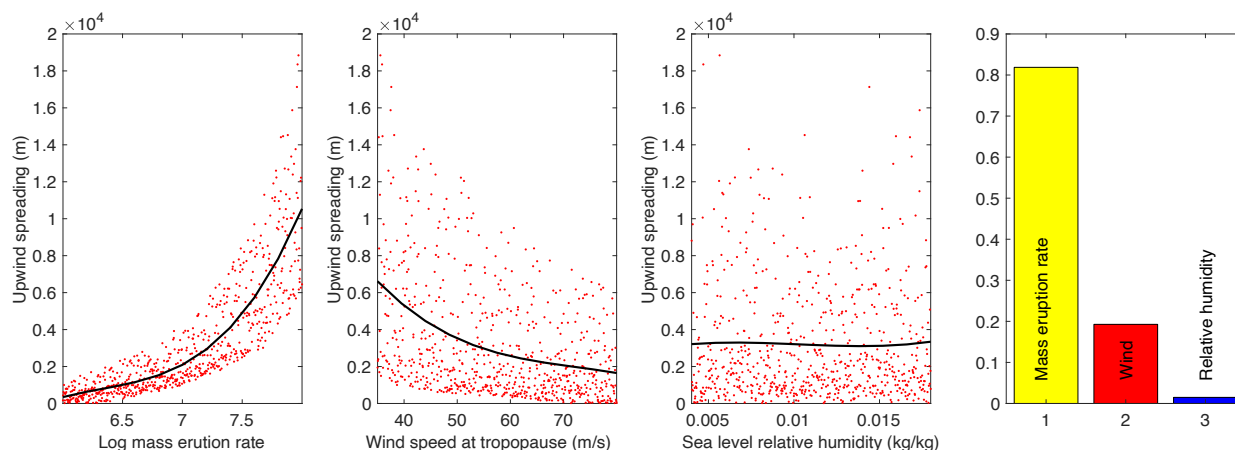


**Figure 10.** Upwind spreading of the umbrella cloud as a function of input parameters (first three panels) and main sensitivity indices (right). In the first three panels each red dot represents a different simulation, whereas the black lines represent the mean of the output parameter at a given input value. For a fixed value of the input parameters on the x-axis of a plot, the vertical spreading of the results is associated with variations in the other input parameters.

The global sensitivity of the upwind spreading with respect to the three input parameters has been computed by using a variance based method (Saltelli et al., 2010; Scollo et al., 2008; de' Michieli Vitturi et al., 2016). If we denote with  $Y$  the output parameter of interest and with  $x_i$  the input parameters considered, the main sensitivity indexes  $S_i$ , also called the Sobol indices, express the fraction of the variability in the output  $Y$ , that is reduced when the value of the input  $x_i$  is fixed. These



indices are calculated by:

$$S_i = \frac{\text{Var}_{x_i}[Y|x_i]}{\text{Var}(Y)}. \quad (46)$$

590 The value of the Sobol indices are shown in the bar plot presented in the right panel of Fig. 10. The largest value is obtained for the sensitivity with respect to the mass flow rate (yellow bar), with a smaller sensitivity with respect to the wind speed at the tropopause (red bar) and a negligible effect of the specific humidity at sea level (blue bar). This highlight the fact the upwind spreading is mostly controlled by the first two parameters.

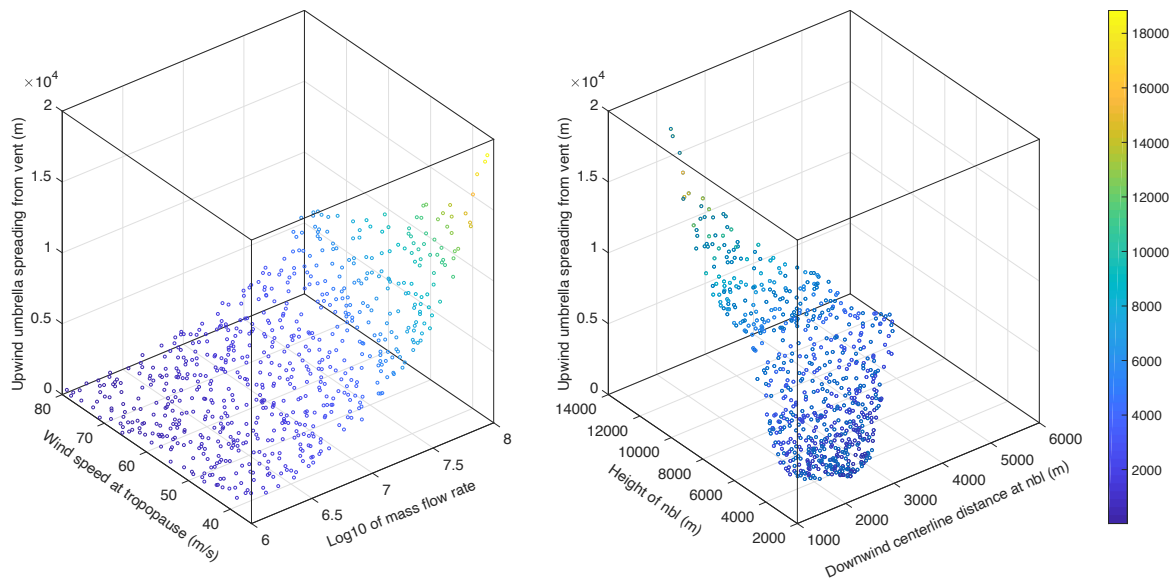


**Figure 11.** Upwind spreading of the umbrella cloud as a function of wind speed at tropopause and mass flow rate (left) and plume model output parameters (right). Please note that in the left panel also the specific humidity at sea level is varied, without producing significant variations in the upwind spreading.

For this reason, we plotted in Fig. 11 the maximum upwind spreading as a function of the logarithm of the mass flow rate and the tropopause wind speed only, highlighting an exponential dependence of the spreading on a linear combination of the two input variables. In fact, if we denote with  $d_{up}$  the upwind spreading and with  $\dot{m}$  and  $v$  the mass flow rate and the tropopause wind speed, respectively, we can write:

$$d_{up} = a \exp(b[-\cos(\theta) \log_{10} \dot{m} - \sin(\theta)v]) \quad (47)$$

A least squares minimization procedure gives as optimal values for the fitting parameters  $a = 0.1495$  m,  $b = -1.601$  and  $\theta = -1.066^\circ$ , with a coefficient of determination  $R^2 = 0.997$  and a square root of the variance of the residuals of 173.1 meters. With these values, the relationship expressed by Eq. (47) gives an estimation of the upwind spreading once the mass flow rate and the tropopause wind speed are known. While from a modeling perspective this represents an interesting result, it is not



always applicable, because the input values needed to compute the spreading cannot be observed directly. For this reason, we plotted in the right panel of Fig. 11 the upwind umbrella distance as a function of the height of the NBL and the downwind horizontal distance from the vent of the centerline, both extracted from the output of PlumeMoM-TSM plume module. As expected, upwind spreading decreases with increasing bending of the column (expressed by the downwind distance of the centerline from the wind), because the bending is associated with wind intensity. On the contrary, upwind spreading increases with increasing height of the intrusion in the atmosphere. Also in this case there is an exponential dependence of the upwind spreading on a linear combination of the two input variables and, if we denote with  $h$  and  $d_{down}$  the NBL height and the downwind distance, respectively, we can write:

$$d_{up} = A \exp(B [-\cos(\Theta)h - \sin(\Theta)d_{down}]). \quad (48)$$

In this case, the least squares minimization procedure gives as optimal values for the fitting parameters  $A = 222.1$  m,  $B = 4.5 \times 10^{-4}$  and  $\Theta = -60.5^\circ$ , with a coefficient of determination  $R^2 = 0.995$  and a square root of the variance of the residuals of 223.3 meters. The results of this fitting and the residuals are shown in Fig. 12, showing that the largest absolute error is obtained for the larger values of the upwind spreading. In any case, these errors of the fitting result in an overestimation of the modeled upwind spreading of less than 3%.

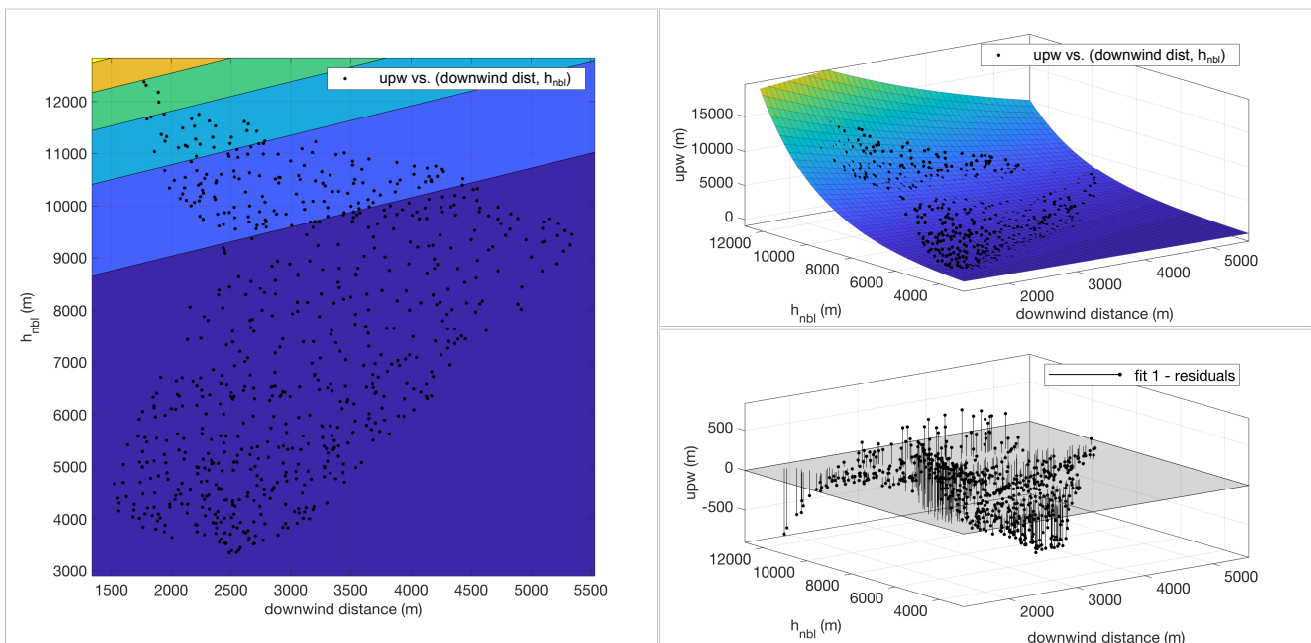


**Figure 12.** Exponential fitting of upwind spreading vs. neutral buoyancy level height and downwind displacement of the plume axis at the same height. A contour plot is shown in the left panel, while on the right a 3D view of the fitting surface (top) and the residuals of the fitting (bottom) are shown. The black dots in the left and top-right panels represent PLUME-MoM-TSM results.



This second relationship, from an operational point of view, results more useful. On one hand, the two input values are produced by all the plume integral model, and in this way a correction can be applied to obtain the upwind spreading without the need of an umbrella cloud spreading model. On the other hand, the input values are also observable data than can be estimated with monitoring techniques, allowing to have an immediate initial estimation of the upwind spreading, and thus of the upwind area potentially affected by the presence of ash, once the volcanic column is observed.

The results presented here are consistent with those discussed in Carey and Sparks (1986), who showed that for very weak plumes no true umbrella cloud forms, and a direct coupling of column and dispersal models is appropriate, and that for column able to reach the tropopause upwind spreading is significant and an umbrella model is required. Finally, it is worth to note that in this analysis we have not varied some of the parameters which can have a large control on the eruptive column, such as the initial water content and temperature (de' Michieli Vitturi et al., 2016; Costa et al., 2016). Further studies will address this point, by considering the uncertainty associated to additional input parameters of the models.

#### 4 Conclusions

PLUME-MoM-TSM, like all the integral models of volcanic plumes, is based on important simplifications, from the steadiness of the plume to the 1D formulation. For this reason, it cannot describe the details of the the complex transient ad 3D dynamics of turbulent volcanic plumes. Despite that, integral models are able to predict column heights and neutral buoyancy levels consistent with those calculated by 3D models (Costa et al., 2016). This result, coupled with the fact the integral models require few seconds to run, pushes toward a further development of these models. In this work we have presented PLUME-MoM-TSM, a new version of the volcanic plume model PLUME-MoM described in de' Michieli Vitturi et al. (2015) and based on the method of moments for the description of the particles distribution. With respect to the previous version, where a finite set of moments of the total grain size distribution were tracked, here the adoption of the two-size moment allowed to model the evolution of the mass and the number of particles associated to each single bin of the distribution. A first important consequence is that, with such approach, it is possible to use PLUME-MoM-TSM outputs as input of VATD models. In addition, the method used in this work to describe the grain size distribution allows for the solution of the full Smoluchowski coagulation equation, and thus to model accurately particle aggregation. We applied here the two-size moment method to the steady-state integral equations for the plume, but the procedure described is general and the code is based on modular structure, which make easy to port the procedure to other Eulerian models for transport of volcanic ash in the atmosphere.

PLUME-MoM-TSM also accounts for phase change of water, resulting in the formation of a liquid water or ice inside the plume, and it includes a module for the spreading of the umbrella cloud as a gravity current. These new features have been tested by applying the model to the April 2015 eruption of Calbuco volcano in Chile, allowing to constrain model parameters and to quantify the effect of wet aggregation on model results. The analysis shows that aggregation has a minimal control on plume characteristics and on the loss of particles from its margins.

Finally, a sensitivity analysis provided a relationship between mass flow rate, wind speed at the tropopause and maximum upwind spreading of the umbrella cloud, and also between observable parameters quantifying plume bending (height of the



650 neutral buoyancy level and downwind displacement of the plume axis at the same height) and the umbrella upwind spreading. These results are in agreement and extend those presented in Carey and Sparks (1986), and provide important information for both modelers and observatories, even if further studies are necessary to extend the analysis to more general initial vent conditions.

*Code availability.* The numerical code, benchmark tests and documentation are available at <https://github.com/demichie/PLUME-MoM-TSM> (last access: 23 June 2020). Postprocessing scripts (to plot the solution variables and to create animations) are also available. Furthermore, each example has a page description on the model Wiki (<https://github.com/demichie/PLUME-MoM-TSM/wiki> (last access: 23 June 2020)), where detailed information on how to run the simulations is given. The digital object identifier (DOI) for the version of the code documented in this paper is <https://doi.org/10.5281/zenodo.3904379> (de' Michieli Vitturi and Pardini, 2020)

## Appendix A: Constitutive equations

### 660 A1 Water phase transition

For the partition of water in the gas, liquid and solid phases, three different cases are considered:  $T_{mix} \geq T_{ref}$ ,  $T_{ref} - 40 < T_{mix} < T_{ref}$  and  $T_{mix} \leq T_{ref} - 40$ , where  $T_{ref}$  is the reference temperature of 273.15 K. Starting from the first case, we solve for the unknown variables (mass fraction of the different phases) and we check if their values are consistent with the hypothesis of thermal and mechanical equilibrium between all phases. If the equilibrium is not possible, we skip to a different case.

665 1. For  $T_{mix} \geq T_{ref}$ , water can be in vapour and liquid form only and  $T_{mix}$  is given by:

$$T_{mix} = \frac{H - x_{lw}(h_{lw0} - C_{lw}T_{ref}) - x_{wv}(h_{wv0} - C_{wv}T_{ref})}{x_{da}C_{atm} + x_sC_s + x_{lw}C_{lw} + x_{wv}C_{wv} + x_{vg}C_{vg}}. \quad (A1)$$

Following Folch et al. (2016), for  $T \geq 29.65$  K, the saturation pressure of vapour over liquid ( $e_l$ ) depends on the temperature in the following way:

$$e_l(T) = 611.2 \exp\left(17.67 \frac{(T - 273.16)}{(T - 29.65)}\right). \quad (A2)$$

670 At equilibrium condition, when both liquid water and vapour are present, it must hold:

$$\Delta_{wv} \equiv P_{wv} - e_l = 0, \quad (A3)$$

where both the terms can be written as functions of  $x_{wv}$ , Eqs. (33c), (34), and (A1).

Before trying to solve Eq. (A3), we consider the two extreme values  $x_{wv} = 0$  (liquid only) and  $x_{wv} = x_w$  (vapour only) in order to check if they are compatible with the condition  $T_{mix} \geq T_{ref}$ . If  $\Delta_{wv}|_{x_{wv}=x_w} < 0$  and  $T_{mix}|_{x_{wv}=x_w} \geq T_{ref}$ , the plume is undersaturated and there is no water vapour condensation ( $x_w = x_{wv}$ ). If  $\Delta_{wv}|_{x_{wv}=0} > 0$  and  $T_{mix}|_{x_{wv}=0} >$

675



$T_{ref}$ , all the water is in liquid form ( $x_w = x_{lw}$ ). Otherwise we apply a bisection iterative method to solve Eq. (A3) for  $x_{wv}$  in the interval  $[0, x_w]$ . Once the solution is obtained, we check if the corresponding temperature, as given by Eq. (A1), is  $\geq T_{ref}$ . If this is not the case,  $T_{mix}$  must be less than  $T_{ref}$ .

680 2. For  $T_{mix} < T_{ref} - 40$ , water can be in vapour and ice form only and the temperature of the eruptive mixture can be computed as:

$$T_{mix} = \frac{H - x_{wv}(h_{wv0} - C_{wv}T_{ref})}{x_{da}C_{atm} + x_sC_s + x_{wv}C_{wv} + x_iC_i + x_{vg}C_{vg}}. \quad (A4)$$

We follow the procedure adopted for  $T_{mix} \geq T_{ref}$  with the difference of considering the equations holding for a mixture containing water as vapour and ice. From Folch et al. (2016), the saturation pressure of vapour over ice ( $e_s$ ) is a function of mixture temperature  $T$  as:

685 
$$e_s(T) = 611.22 \cdot 10^{-9.097\left(\frac{273.16}{T} - 1\right) - 3.566 \log_{10}\left(\frac{273.16}{T}\right) + 0.876\left(1 - \frac{T}{273.16}\right)}. \quad (A5)$$

At equilibrium, when both vapour and ice are present, it must hold:

$$\Delta_{wv} \equiv P_{wv} - e_s = 0, \quad (A6)$$

690 where  $P_{wv}$  and  $e_s$  are functions of  $x_{wv}$  only, Eqs. (33c), (34), and (A4). Again, before solving Eq. (A6), we examine the two extreme cases:  $x_{wv} = 0$  (ice only) and  $x_{wv} = x_w$  (vapour only) and we check if the corresponding temperature as evaluated from Eq. (A4) is less than  $T_{ref} - 40$ . In case  $\Delta_{wv}|_{x_{wv}=x_w} < 0$  and  $T_{mix}|_{x_{wv}=x_w} < T_{ref} - 40$ , the plume is undersaturated and water is in vapour form only ( $x_w = x_{wv}$ ). On the contrary, in case  $\Delta_{wv}|_{x_{wv}=0} > 0$  and  $T_{mix}|_{x_{wv}=0} < T_{ref} - 40$  all the water is present as ice ( $x_w = x_i$ ).

If equilibrium conditions can not be obtained for the two extreme cases, we solve Eq. (A6) for  $x_w$  by applying a bisection procedure in the interval  $[0, x_w]$  and we check if the corresponding temperature given by Eq. (A4) is  $< T_{ref} - 40$ .

695 3. For  $T_{ref} - 40 < T_{mix} < T_{ref}$ , water can be in vapour, liquid and ice form. Following Mastin (2007) and references therein, we assume that in this range of temperatures liquid and ice coexist but not in equilibrium, with liquid water present in a subcooled state to temperatures well below freezing. In this case, specific mixture enthalpy can be computed from Eq. (27) as a function of mixture temperature only. Indeed, we show in the following that water mass fractions can be written as functions of  $T_{mix}$ . Water vapour mass fraction is computed by inverting Eq. (34) as:

700 
$$x_{wv}(T_{mix}) = -\frac{\left(\frac{x_{da}}{mw_{da}} + \frac{x_{vg}}{mw_{vg}}\right)n_{wv}mw_{wv}}{(mw_{wv} - 1)}. \quad (A7)$$

The right-hand side term contains  $n_{wv}$  which, at this stage, is unknown. However, at equilibrium conditions,  $n_{wv}$  is a function of  $T_{mix}$  and it can be computed by inverting Eq. (33) as:

$$n_{wv} = \frac{e|_{T=T_{mix}}}{P_{atm}}, \quad (A8)$$



705 where  $e$  is vapour partial pressure which, depending on mixture temperature, can be evaluated from Eq. (A2) for  $T_{mix} = T_{ref}$  or from Eq. (A5) for  $T_{mix} = T_{ref} - 40$ .

As done in Mastin (2007), we assume that liquid water mass fraction is a function of  $T_{mix}$  as:

$$x_{lw}(T_{mix}) = x_{lw}|_{T_{mix}=T_{ref}} \left[ \frac{T_{mix} - (T_{ref} - 40)}{40} \right], \quad (\text{A9})$$

where  $x_{lw}|_{T_{mix}=T_{ref}}$  can be computed from  $x_{wv}|_{T_{mix}=T_{ref}}$  assuming that at  $T_{ref}$  no ice is present. Finally, ice mass fraction is:

710 
$$x_i(T_{mix}) = x_w - x_{wv} - x_{lw}. \quad (\text{A10})$$

The specific enthalpy of the eruptive mixture at equilibrium ( $H_{eq}$ ) is known by solving the energy equation, and, for a generic mixture temperature  $\bar{T}$ , it must hold:

$$\Delta_H \equiv H_{eq} - H|_{T_{mix}=\bar{T}} = 0, \quad (\text{A11})$$

715 where  $H|_{T_{mix}=\bar{T}}$  is the mixture enthalpy at the generic temperature  $\bar{T}$ . Before solving Eq. (A11) we check if equilibrium is possible in the interval  $[T_{ref}-40, T_{ref}]$  by computing  $\Delta_H|_{T_{mix}=T_{ref}-40}$  and  $\Delta_H|_{T_{mix}=T_{ref}}$ . If  $\Delta_H|_{T_{mix}=T_{ref}-40} > 0$  and  $\Delta_H|_{T_{mix}=T_{ref}} > 0$  or  $\Delta_H|_{T_{mix}=T_{ref}-40} < 0$  and  $\Delta_H|_{T_{mix}=T_{ref}} < 0$ , it means that that equilibrium can not be reached in the range  $[T_{ref} - 40, T_{ref}]$  and we examine the case  $T_{mix} < T_{ref} - 40$ . Otherwise we apply a bisection procedure to solve for  $T_{mix}$  and water partitions in the interval  $[T_{ref} - 40, T_{ref}]$ . During the procedure, we check that water partitions are positive values and their sum is equal to water mass fraction. In case these conditions are not hold, 720 we skip to a different case.

## A2 Settling velocity

Several models are implemented in PLUME-MoM-TSM to compute particle settling velocity ( $w_{i_p}$ ) as a function of particle diameter ( $D$ ), particle density ( $\rho_p$ ) and shape factor ( $\psi$ ).

The first model is taken from Textor et al. (2006b) and references therein:

725 
$$w_{i_p}(D) = \begin{cases} k_1 \rho_p \sqrt{\frac{\rho_{atm0}}{\rho_{atm}}} \left(\frac{D}{2}\right)^2, & D \leq 100 \mu\text{m}. \\ k_2 \rho_p \sqrt{\frac{\rho_{atm0}}{\rho_{atm}}} \left(\frac{D}{2}\right), & 100 \mu\text{m} < D \leq 1000 \mu\text{m} \\ k_3 \sqrt{\frac{\rho_p}{C_D}} \sqrt{\frac{\rho_{atm0}}{\rho_{atm}}} \sqrt{\frac{D}{2}}, & D > 1000 \mu\text{m}. \end{cases} \quad (\text{A12})$$

where  $k_1 = 1.19 \times 10^5 \text{ m}^2 \text{ kg}^{-1} \text{ s}^{-1}$ ,  $k_2 = 8 \text{ m}^3 \text{ kg}^{-1} \text{ s}^{-1}$ ,  $k_3 = 4.833 \text{ m}^2 \text{ kg}^{-1/2} \text{ s}^{-1}$  and  $C_D$  is the drag coefficient that we set equal to 0.75.



The second model (Ganser, 1993) defines the settling velocity for the Stokes' regime ( $Re \ll 0.005$ ) as:

$$w_{i_p}(D) = \sqrt{\frac{4gD(\rho_p - \rho_{atm})}{3C_D\rho_{atm}}}. \quad (\text{A13})$$

730 The drag coefficient ( $C_D$ ) in Eq.A13 is calculated with the following expression:

$$C_D = \frac{24}{ReK_1}(1 + 0.1118(ReK_1K_2)^{0.6567}) + \frac{0.4305K_2}{1 + \frac{3305}{ReK_1K_2}}, \quad (\text{A14})$$

where  $Re$  is the Reynolds number,  $K_1$  is the Stokes' shape factor and  $K_2$  is the Newton's shape factor:

$$Re = \frac{\rho_{atm}w_{i_p}(D)D}{\mu}, \quad (\text{A15})$$

$$K_1 = \frac{3}{1 + 2\psi^{-0.5}}, \quad (\text{A16})$$

735 
$$K_2 = 10^{1.8148(-\log\psi)^{0.5743}}. \quad (\text{A17})$$

Finally, settling velocity can be computed following Pfeiffer et al. (2005) as:

$$w_{i_p}(D) = \sqrt{\frac{2mg}{C_D\rho_{atm}A_{cs}}}, \quad (\text{A18})$$

where  $m$  is the particle mass and  $A_{cs}$  the cross-sectional area of the particle. Depending on the Reynolds number, the drag coefficient used in Eq. (A18) is:

740 
$$C_D = \begin{cases} \frac{24}{Re}\psi^{-0.828} + 2\sqrt{1.07 - \psi}, & Re \leq 100. \\ C_{DRe_{100}} + \frac{(Re-100)}{1000-100}(C_{DRe_{1000}} - C_{DRe_{100}}), & 100 \leq Re < 1000 \\ 1, & Re > 1000. \end{cases} \quad (\text{A19})$$

We remark here that the Reynolds number is a function of the settling velocity, and thus for the formulations where the drag coefficient is a function of the Reynolds number a nonlinear equation has to be solved. This is done in PLUME-MoM-TSM with an iterative procedure.



### A3 Aggregation kernel

745 Following Costa et al. (2010), a model for wet aggregation based on the classical Smoluchowski equation is implemented in PLUME-MoM-TSM. In their work, a general model describing the aggregation processes was presented, but a simplified version computationally cheaper was then adopted. Here, the full original version is retained and implemented in the plume model, according with the framework of the TSM method of moments.

750 The kernel aggregation is defined as the product of a collision frequency function  $\delta_{ij}$  and a sticking efficiency function  $\lambda_{ij}$ , with the collision frequency function given by the sum of three contributions: a Brownian frequency function  $\delta_B$ ; a fluid shear frequency function  $\delta_S$ ; and a differential sedimentation frequency function  $\delta_{DS}$ . Considering two particles of the family  $i_p$  with masses  $m_i$  and  $m_j$  and diameters in meters  $d_i$  and  $d_j$ , we can write

$$\delta = \delta_B + \delta_S + \delta_{DS} = \frac{2}{3} \frac{k_b T_{mix}}{\mu} \frac{(d_i + d_j)^2}{d_i d_j} + \frac{1}{6} \Gamma_S (d_i + d_j)^3 + \frac{\pi}{4} (d_i + d_j)^2 |w_{i_p}(d_i) - w_{i_p}(d_j)| \quad (\text{A20})$$

where  $k_b$  is the Boltzmann constant,  $\mu$  is the dynamic viscosity of air, and  $\Gamma_S$  is the fluid shear.

755 Following Costa et al. (2010), sticking efficiency  $\lambda_{ij}$  in presence of ice only (no liquid water) takes a constant value:

$$\lambda_{ij}^i = 0.09. \quad (\text{A21})$$

When liquid water is present in the plume (without ice), sticking is a function of the viscous Stokes number  $St_{ij}$  (Costa et al., 2010; Liu and Litster, 2002), and the following parametrization is adopted:

$$\lambda_{ij}^{lw} = \frac{1}{1 + \left(\frac{St_{ij}}{St_{cr}}\right)^q} \quad (\text{A22})$$

760 where  $St_{cr} = 1.3$  is a critical Stokes number above which there is no sticking, and  $q = 0.8$  is an empirical parameter. These two expressions for sticking efficiency do not take into account the amount of ice/liquid water available in the plume as limiting factor for aggregation. Here, we modified the formulation presented in Costa et al. (2010), by taking the sticking efficiency as a weighted linear combination of the two expressions above:

$$\lambda_{ij} = \alpha_{lw} \lambda_{ij}^{lw} + \alpha_i \lambda_{ij}^i, \quad (\text{A23})$$

765 where  $\alpha_{lw}$  and  $\alpha_i$  are the volumetric fraction of liquid water and ice in the mixture, respectively.

### Appendix B: Addition of external water

To test the consistency of our results with those presented by Koyaguchi and Woods (1996) and later by Mastin (2007) for the addition of external water at the base of the plume, we applied PLUME-MoM-TSM to reproduce some of the figures presented in their works. The left panel of Fig. B1 shows the effects of external water on plume height as a function of mass  
 770 flow rate. PLUME-MoM-TSM results (orange lines) are compared with those of Plumeria (light blue lines digitized from Fig.



C4 of Mastin (2007)) and those of Koyaguchi and Woods (1996) (green lines digitized from Fig. 5). It can be seen a general agreement between our results and those of the other models, with a maximum difference of 20% between the maximum column height found by PLUME-MoM-TSM and the one found by Plumeria for the 10% external water case. For the 0% case, PLUME-MoM-TSM predicts column collapse for a slightly lower mass eruption rate than the other models, while a good fit  
 775 between PLUME-MoM-TSM and Koyaguchi and Woods (1996) results is observed for the other cases.

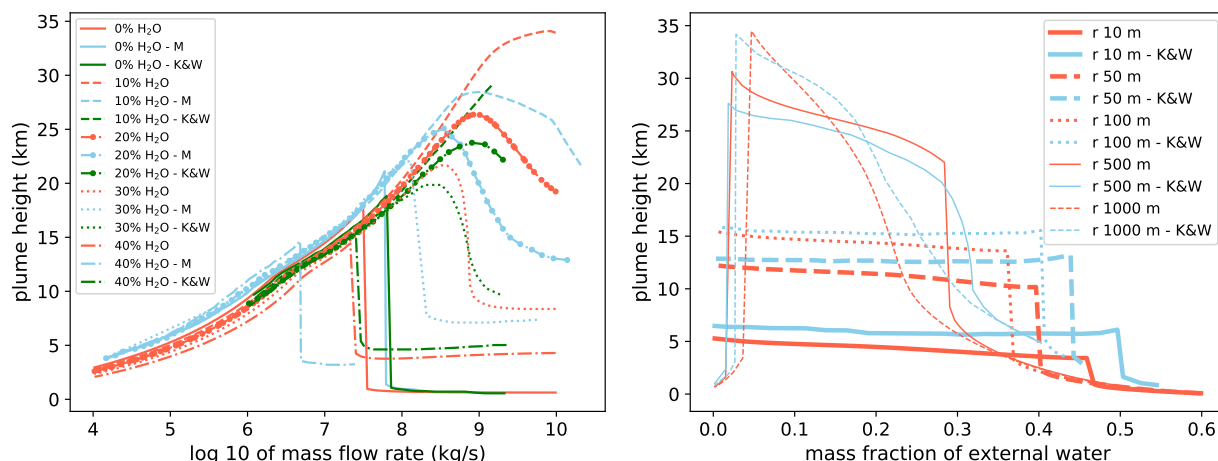


**Figure B1.** LEFT PANEL: effect of addition of external water on column height as a function of mass flow rate. As in Koyaguchi and Woods (1996) and Mastin (2007), input parameters are: magma temperature = 1000 K, water vapour mass fraction = 0.03 wt and relative humidity in the atmosphere = 100%. The exit velocity for the dry scenario is  $100 \text{ m s}^{-1}$ , while an adjustment on exit velocities was done for the runs with external water to match the mass flux of magma and gas of the dry case. For this reason, exit velocities are 300, 329, 289 and  $236 \text{ m s}^{-1}$  for the runs involving 10%, 20%, 30% and 40% of external water, respectively (Mastin, 2007). RIGHT PANEL: plume height as a function of mass fraction of external water added at the vent. Orange lines show the PLUME-MoM-TSM results, while light blue lines are digitized from Fig. 4 of Koyaguchi and Woods (1996). Curves are shown for vent radii of 10, 50, 100, 500 and 1000 m. Exit velocity is equal to  $100 \text{ m s}^{-1}$ , water vapour content to 0.03 wt and mixture temperature to 1000 K.

The right panel of Fig. B1 reproduces Fig. 4 of Koyaguchi and Woods (1996), where it is shown the height of the eruptive column as a function of the mass of external water added at the vent. Each curve is drawn for a constant mass flow rate of  $2.24 \times 10^5$ ,  $5.6 \times 10^6$ ,  $2.24 \times 10^7$ ,  $5.6 \times 10^8$  and  $2.24 \times 10^9 \text{ kg s}^{-1}$ . These values correspond to vent radii of 10, 50, 100, 500 and 1000 m, respectively. The PLUME-MoM-TSM results (orange lines) appear to be similar to those of (Koyaguchi and Woods, 1996) (light blue lines), although PLUME-MoM-TSM predicts column collapse for slightly lower values of external water than Koyaguchi and Woods (1996). Fig. B2 and B3 present the variation of mixture temperature, velocity, relative density, gas mass fraction and water mass fraction (liquid and ice) as functions of column height for two eruptive scenarios. Each panel shows the results for amounts of external water of 3, 10, 20 and 30 wt%. The two figures reproduce Fig. 3 of Koyaguchi and Woods (1996).  
 780

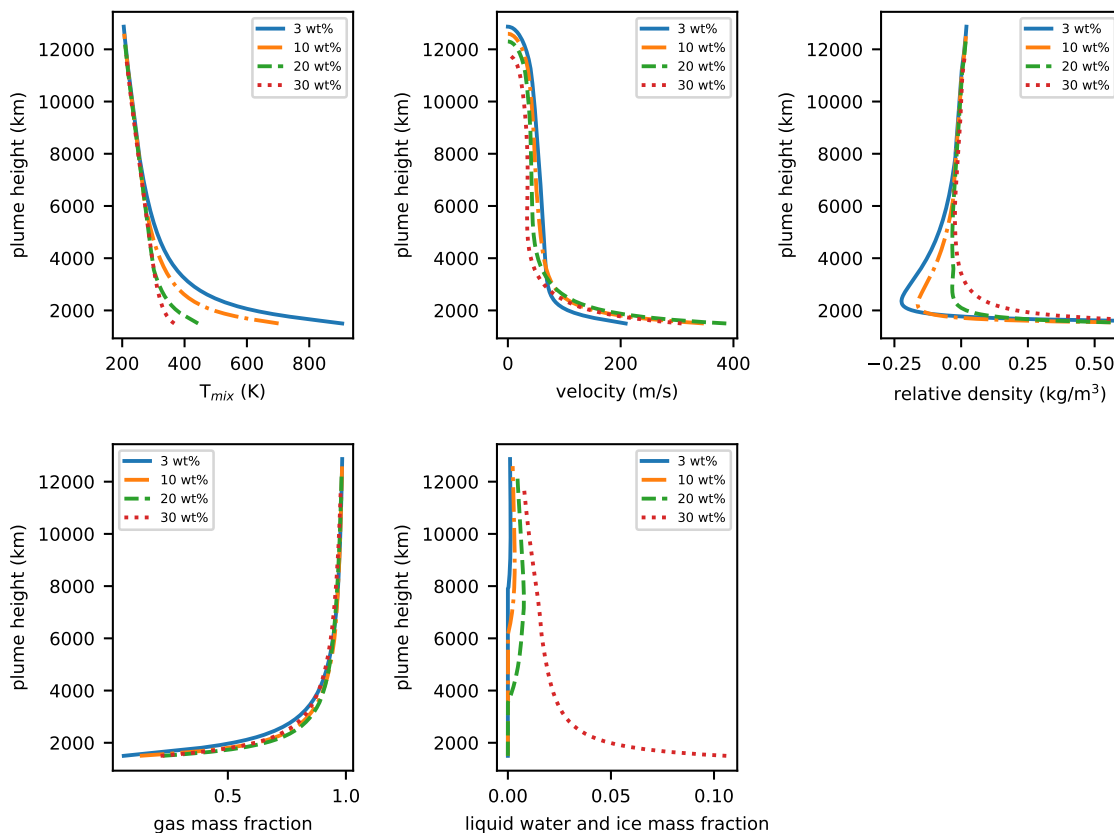


**Figure B2.** Variation with column height of mixture temperature, velocity, relative density, gas mass fraction and liquid+ice mass fraction. As done in Koyaguchi and Woods (1996), each curve accounts for a different amount of external water added to the magmatic mixture: 3, 10, 20, 30 wt%. The dry case is set for a vent radius of 50 m and an exit velocity of  $100 \text{ m s}^{-1}$ , resulting in a mass flow rate of  $5.7 \times 10^6 \text{ kg s}^{-1}$ . The wet cases are obtained by keeping constant vent radius and mass flow rate, while varying exit velocity. Magma is assumed to contain 0.03 wt fraction of volatiles (only water vapour) and to have an initial temperature of 1000 K.

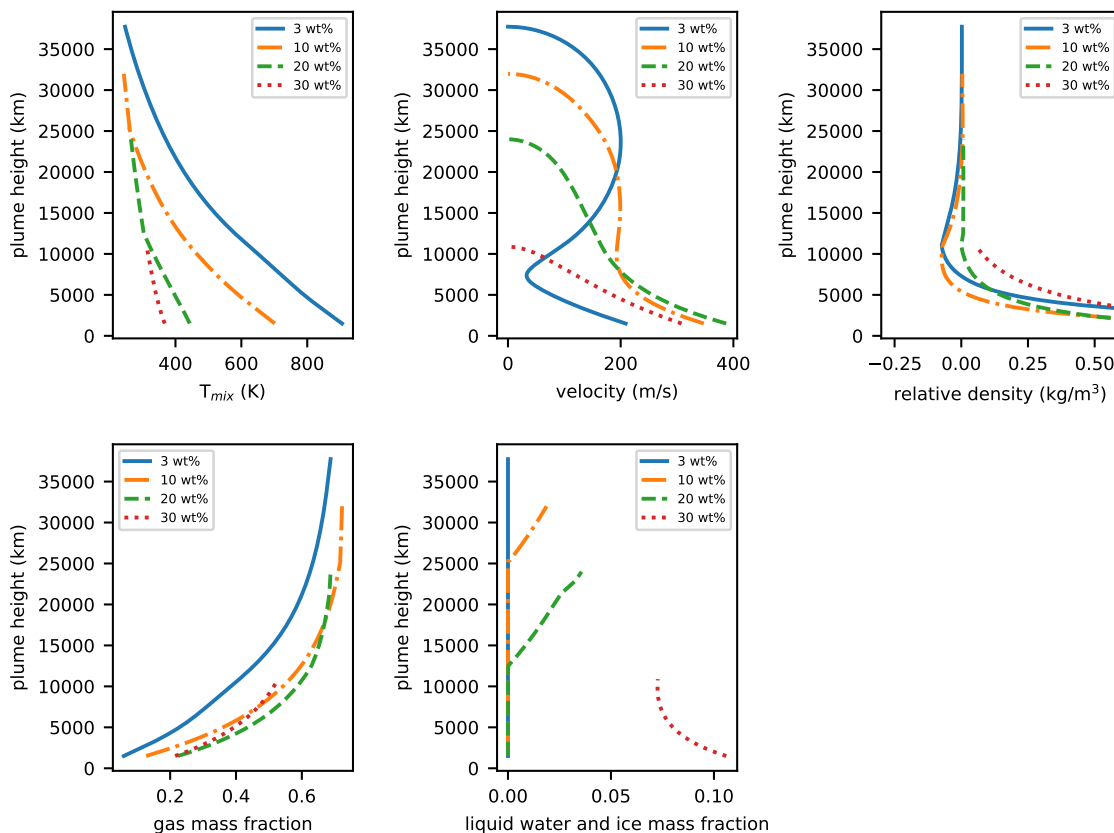


**Figure B3.** As in Fig. B2, but the model is initialized with a vent radius of 1000 m.

785 Following Koyaguchi and Woods (1996), Fig. B4 shows the variation of initial mixture density and temperature as the mass of external liquid water increases. The figure shows how the addition of a certain amount of external water alters the properties of the magmatic mixture at the vent. The three curves are done for different initial temperatures of the eruptive mixture (1000 and 1400 K) and volatile contents (0.01 and 0.05 wt fraction, only water vapour is considered). The temperature of the external water is 273 K.

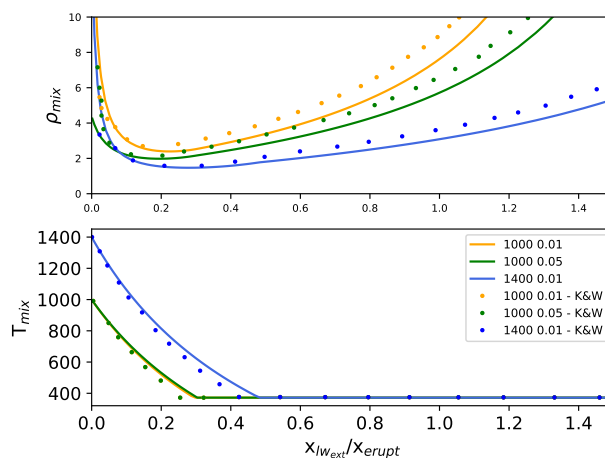


**Figure B4.** Variation of initial mixture density ( $\rho_{mix}$ ) and temperature ( $T_{mix}$ ) as the mass of water added to the magma is increased. Continuous lines show the results of PLUME-MoM, while dotted lines are digitized from Koyaguchi and Woods (1996). Curves are shown for initial magma temperatures of 1000 and 1400 K, while magma volatile content ranges from 0.01 to 0.05 wt fraction.

## 790 Appendix C: List of model variables



**Table C1.** List of Symbols

Symbol	Definition	Units	Comments
$C_{atm}$	Specific heat capacity of air	$Jkg^{-1}K^{-1}$	
$C_D$	Drag coefficient		
$C_{lw}$	Specific heat capacity of liquid water	$Jkg^{-1}K^{-1}$	= 4187
$C_i$	Specific heat capacity of ice	$Jkg^{-1}K^{-1}$	= 2108
$C_s$	Specific heat capacity of the solid phase	$Jkg^{-1}K^{-1}$	
$C_{s,i_p}$	Specific heat capacity of $i$ -th particle family	$Jkg^{-1}K^{-1}$	
$C_{vg}$	Specific heat capacity of volcanic gases	$Jkg^{-1}K^{-1}$	
$C_{wv}$	Specific heat capacity water vapour	$Jkg^{-1}K^{-1}$	= 1996
$E$	Total specific energy	$Jkg^{-1}$	
$e_s$	Saturation pressure of water vapour over ice	$Pa$	
$e_l$	Saturation pressure of water vapour over liquid	$Pa$	
$g$	Gravitational acceleration	$ms^{-2}$	= 9.81
$H$	Specific enthalpy	$Jkg^{-1}$	
$H_{vent}$	Specific enthalpy at the vent without addition of external liquid water	$Jkg^{-1}$	
$H_{vent_{new}}$	Specific enthalpy at the vent after addition of external liquid water	$Jkg^{-1}$	
$h$	Thickness of umbrella cloud intrusion	$m$	
$h_{lw0}$	Enthalpy per unit mass of liquid water at $T_{ref}$	$Jkg^{-1}$	= $3.337 \times 10^{-5}$
$h_{wv0}$	Enthalpy per unit mass of water vapour at $T_{ref}$	$Jkg^{-1}$	= $2.501 \times 10^6$
$mw_{da}$	Dry air molar weight	$kgmole^{-1}$	= 0.029
$mw_k$	$k$ -th volcanic gas phase molar weight	$kgmole^{-1}$	
$mw_{vg}$	Volcanic gas molar weight	$kgmole^{-1}$	
$mw_{wv}$	Water vapour molar weight	$kgmole^{-1}$	= 0.018
$N$	Brunt-Väisälä frequency	$s^{-1}$	
$n_{da}$	Dry air molar fraction		
$n_{vg}$	Volcanic gas molar fraction		
$n_{wv}$	Water vapour molar fraction		
$p$	Probability of particle loss	–	
$P_{atm}$	Atmospheric pressure	$Pa$	
$P_{da}$	Partial pressure of dry air	$Pa$	
$P_{vg}$	Partial pressure of volcanic gases	$Pa$	
$P_{wv}$	Partial pressure of water vapour	$Pa$	
$r$	Plume radius	$m$	



**Table C1.** Continued.

Symbol	Definition	Units	Comments
$R_{air}$	Specific gas constant of dry air	$Jkg^{-1}K^{-1}$	$= 287.026$
$R_{wv}$	Specific gas constant of water vapour	$Jkg^{-1}K^{-1}$	$= 462$
$T_{atm}$	Atmospheric temperature	$K$	
$T_{lw_{ext}}$	Temperature of external liquid water	$K$	
$T_{mix}$	Mixture Temperature	$K$	
$T_{ref}$	Reference Temperature	$K$	$= 273.15K$
$T_{mix0}$	Temperature of the magma	$K$	
$u$	Horizontal x-component of plume velocity	$ms^{-1}$	
$u_a$	Horizontal x-component of atmospheric wind	$ms^{-1}$	
$U_{atm}$	Magnitude of atmospheric wind	$ms^{-1}$	
$U_{\epsilon}$	Air entrainment velocity	$ms^{-1}$	
$U_{sc}$	Magnitude of plume velocity	$ms^{-1}$	$= \sqrt{u^2 + v^2 + w^2}$
$v$	Horizontal y-component of plume velocity	$ms^{-1}$	
$v_a$	Horizontal y-component of atmospheric wind	$ms^{-1}$	
$w$	Vertical plume velocity	$ms^{-1}$	
$w_{atm}$	Specific humidity	$kgkg^{-1}$	
$w_{ip}$	Particle settling velocity	$ms^{-1}$	
$x$	Horizontal coordinate	$m$	
$x_{da}$	Mass fraction of dry air		
$x_{erupt}$	Mass fraction of eruptive mixture without external liquid water		
$x_i$	Mass fraction of ice		
$x_k$	Mass fraction of $k$ -th volcanic gas	–	
$x_{lw}$	Mass fraction of liquid water		
$x_{lw_{ext}}$	Mass fraction of external liquid water added at the vent		
$x_s$	Mass fraction of solid particles	–	
$x_{vg}$	Mass fraction of volcanic gases in the mixture		
$x_w$	Mass fraction of water		$= x_{wv} + x_l + x_i$
$x_{wv}$	Mass fraction of water vapour	–	
$y$	Horizontal coordinate	$m$	
$z$	Vertical coordinate	$m$	



**Table C1.** Continued.

Symbol	Definition	Units	Comments
$\alpha_\epsilon$	Radial entrainment coefficient	–	
$\beta$	Aggregation kernel	$m^3 s^{-1}$	
$\Gamma_{atm}$	Moist atmospheric lapse rate	$K m^{-1}$	
$\Gamma_d$	Dry atmospheric lapse rate	$K m^{-1}$	
$\gamma_\epsilon$	Cross-flow air entrainment coefficient	–	
$\delta$	Collision frequency	$m^3 s^{-1}$	
$\lambda$	Sticking efficiency		
$\rho_{atm}$	Air density	$kg m^{-3}$	
$\rho_d$	Dry air density	$kg m^{-3}$	
$\rho_{mix}$	Density of the mixture	$kg m^{-3}$	Solid particles and gas
$\phi$	Diameter in Krumbein scale	–	
$\psi$	Particle shape factor	–	

*Author contributions.* Both the authors equally contributed to the model development, the numerical simulations, the analysis of the results and the preparation of the manuscript.

*Competing interests.* The authors declare no competing interests.

795 *Acknowledgements.* This work has been supported by the Italian Department of Civil Protection, INGV-DPC agreement A 2020. FP research activities were partially funded by the Italian MIUR project Premiale Ash-RESILIENCE, the MIUR FISR project "Sale Operative Integrate e Reti di Monitoraggio del Futuro", and the European project EUROVOLC (grant number 731070). The authors also thank Alessandro Tadini, Kyle Mohr and Silvia Giansante for testing of the code and for the feedbacks provided and Giovanni Biagioli for the help in the definition of the modified standard atmosphere.



## References

- 800 Abramowitz, M. and Stegun, I. A.: Handbook of mathematical functions with formulas, graphs, and mathematical table, in: US Department of Commerce, National Bureau of Standards Applied Mathematics series 55, 1965.
- Ahrens, C. D.: Meteorology today: an introduction to weather, climate, and the environment, Cengage Learning, 2012.
- Anderson, G. P., Clough, S. A., Kneizys, F., Chetwynd, J. H., and Shettle, E. P.: AFGL atmospheric constituent profiles (0.120 km), Tech. rep., AIR FORCE GEOPHYSICS LAB HANSCOM AFB MA, 1986.
- 805 Ascher, U. M., Ruuth, S. J., and Spiteri, R. J.: Implicit-explicit Runge-Kutta methods for time-dependent partial differential equations, *Applied Numerical Mathematics*, 25, 151–167, 1997.
- Baines, P. G.: The dynamics of intrusions into a density-stratified crossflow, *Physics of Fluids*, 25, 076 601, 2013.
- Bonadonna, C., Biass, S., Menoni, S., and Gregg, C. E.: Assessment of risk associated with tephra-related hazards, in: *Forecasting and Planning for Volcanic Hazards, Risks, and Disasters*, edited by Papale, P., Elsevier, 1 edn., 2020.
- 810 Brasefield, C.: Winds at altitudes up to 80 kilometers, *Journal of Geophysical Research*, 59, 233–237, 1954.
- Brown, R., Bonadonna, C., and Durant, A.: A review of volcanic ash aggregation, *Physics and Chemistry of the Earth, Parts A/B/C*, 45, 65–78, 2012.
- Bursik, M.: Effect of wind on the rise height of volcanic plumes, *Geophys. Res. Lett.*, 18, 3621–3624, 2001.
- Carey, S. and Sparks, R.: Quantitative models of the fallout and dispersal of tephra from volcanic eruption columns, *Bulletin of Volcanology*,
- 815 48, 109–125, 1986.
- Castruccio, A., Clavero, J., Segura, A., Samaniego, P., Roche, O., Le Pennec, J.-L., and Droguett, B.: Eruptive parameters and dynamics of the April 2015 sub-Plinian eruptions of Calbuco volcano (southern Chile), *Bulletin of Volcanology*, 78, 62, 2016.
- Cerminara, M., Ongaro, T. E., and Berselli, L. C.: ASHEE: a compressible, equilibrium-Eulerian model for volcanic ash plumes, arXiv preprint arXiv:1509.00093, 2015.
- 820 Colucci, S., Landi, P., and de' Michieli Vitturi, M.: CrystalMom: a new model for the evolution of crystal size distributions in magmas with the quadrature-based method of moments, *Contributions to Mineralogy and Petrology*, 172, 100, 2017.
- Costa, A., Folch, A., and Macedonio, G.: A model for wet aggregation of ash particles in volcanic plumes and clouds: 1. Theoretical formulation, *Journal of Geophysical Research: Solid Earth (1978–2012)*, 115, 2010.
- Costa, A., Folch, A., and Macedonio, G.: Density-driven transport in the umbrella region of volcanic clouds: Implications for tephra disper-
- 825 sion models, *Geophysical Research Letters*, <http://onlinelibrary.wiley.com/doi/10.1002/grl.50942/full>, 2013.
- Costa, A., Suzuki, Y. J., Cerminara, M., Devenish, B. J., Ongaro, T. E., Herzog, M., Van Eaton, A. R., Denby, L., Bursik, M., Vitturi, M. d., et al.: Results of the eruptive column model inter-comparison study, *Journal of Volcanology and Geothermal Research*, 326, 2–25, 2016.
- Daidzic, N. E.: On atmospheric lapse rates, *International Journal of Aviation, Aeronautics, and Aerospace*, 6, 2, 2019.
- de' Michieli Vitturi, M. and Pardini, F.: PLUME-MoM-TSM v. 1.0.0 (Version 1.0.0), Tech. rep., <https://doi.org/10.5281/zenodo.3904379>,
- 830 <http://https://zenodo.org/record/3904379>, 2020.
- de' Michieli Vitturi, M., Neri, A., and Barsotti, S.: PLUME-MoM 1.0: A new integral model of volcanic plumes based on the method of moments, *Geosci. Model Dev.*, 8, 2447–2463, <https://doi.org/10.5194/gmd-8-2447-2015>, <http://dx.doi.org/10.5194/gmd-8-2447-2015>, 2015.



- de' Michieli Vitturi, M., Engwell, S., Neri, A., and Barsotti, S.: Uncertainty quantification and sensitivity analysis of volcanic columns models: Results from the integral model PLUME-MoM, *Journal of Volcanology and Geothermal Research*, <https://doi.org/doi:10.1016/j.jvolgeores.2016.03.014>, 2016.
- de' Michieli Vitturi, M., Esposti Ongaro, T., Lari, G., and Aravena, A.: IMEX\_SfloW2D 1.0: a depth-averaged numerical flow model for pyroclastic avalanches, *Geoscientific Model Development*, 12, 581–595, 2019.
- Degruyter, W. and Bonadonna, C.: Improving on mass flow rate estimates of volcanic eruptions, *Geophysical Research Letters*, 39, 2012.
- 835 Devenish, B.: Using simple plume models to refine the source mass flux of volcanic eruptions according to atmospheric conditions, *Journal of volcanology and geothermal research*, 256, 118–127, 2013.
- Dormand, J. R. and Prince, P. J.: A family of embedded Runge-Kutta formulae, *Journal of computational and applied mathematics*, 6, 19–26, 1980.
- Dutton, J. A.: *The ceaseless wind: An introduction to the theory of atmospheric motion*, Courier Corporation, 2002.
- 845 Folch, A., Costa, A., and Macedonio, G.: FPLUME-1.0: An integral volcanic plume model accounting for ash aggregation, *Geoscientific Model Development*, 9, 431, 2016.
- Ganser, G. H.: A rational approach to drag prediction of spherical and nonspherical particles, *Powder Technology*, 77, 143–152, 1993.
- Graf, H.-F., Herzog, M., Oberhuber, J. M., and Textor, C.: Effect of environmental conditions on volcanic plume rise, *Journal of Geophysical Research: Atmospheres*, 104, 24 309–24 320, 1999.
- 850 Herzog, M., Graf, H.-F., Textor, C., and Oberhuber, J. M.: The effect of phase changes of water on the development of volcanic plumes, *Journal of Volcanology and Geothermal Research*, 87, 55–74, 1998.
- Hewett, T., Fay, J., and Hoult, D.: Laboratory experiments of smokestack plumes in a stable atmosphere, *Atmospheric Environment (1967)*, 5, 767–789, 1971.
- Johnson, C. G., Hogg, A. J., Huppert, H. E., Sparks, R. S. J., Phillips, J. C., Slim, A. C., and Woodhouse, M. J.: Modelling intrusions through quiescent and moving ambients, *Journal of Fluid Mechanics*, 771, 370–406, 2015.
- 855 Koyaguchi, T. and Woods, A. W.: On the formation of eruption columns following explosive mixing of magma and surface-water, *Journal of Geophysical Research: Solid Earth*, 101, 5561–5574, 1996.
- Künzli, P., Falcone, J.-L., Rossi, E., Albuquerque, P., and Chopard, B.: HPC multiscale simulation of transport and aggregation of volcanic particles, in: 2018 17th International Symposium on Parallel and Distributed Computing (ISPDC), pp. 25–32, IEEE, 2018.
- 860 Liu, L. and Litster, J.: Population balance modelling of granulation with a physically based coalescence kernel, *Chemical Engineering Science*, 57, 2183–2191, 2002.
- Marchisio, D. L. and Fox, R. O.: *Computational models for polydisperse particulate and multiphase systems*, Cambridge University Press, 2013.
- Marchisio, D. L., Vigil, R. D., and Fox, R. O.: Quadrature method of moments for aggregation–breakage processes, *Journal of colloid and interface science*, 258, 322–334, 2003.
- 865 Mastin, L. G.: A user-friendly one-dimensional model for wet volcanic plumes, *Geochemistry, Geophysics, Geosystems*, 8, 2007.
- Modica, G. D., Nehr Korn, T., and Myers, T.: An Investigation of Stratospheric Winds in Support of the High Altitude Airship, available at: [ams.confex.com/ams/pdfpapers/128256.pdf](https://ams.confex.com/ams/pdfpapers/128256.pdf) (last access: September 2010), 2007.
- Morton, B., Taylor, G., and Turner, J.: Turbulent gravitational convection from maintained and instantaneous sources, in: *Proceedings of the Royal Society of London A: Mathematical, Physical and Engineering Sciences*, vol. 234, pp. 1–23, The Royal Society, 1956.
- 870



- Nguyen, T. T., Laurent, F., Fox, R. O., and Massot, M.: Solution of population balance equations in applications with fine particles: mathematical modeling and numerical schemes, *Journal of Computational Physics*, 325, 129–156, 2016.
- Oberhuber, J. M., Herzog, M., Graf, H.-F., and Schwanke, K.: Volcanic plume simulation on large scales, *Journal of Volcanology and Geothermal Research*, 87, 29–53, 1998.
- 875 Ongaro, T. E., Cavazzoni, C., Erbacci, G., Neri, A., and Salvetti, M.-V.: A parallel multiphase flow code for the 3D simulation of explosive volcanic eruptions, *Parallel Computing*, 33, 541–560, 2007.
- Þórarinnsson, S.: *Surtsey: the new island in the North Atlantic*, Viking Press, 1967.
- Pardini, F., Burton, M., Arzilli, F., La Spina, G., and Polacci, M.: SO<sub>2</sub> emissions, plume heights and magmatic processes inferred from satellite data: The 2015 Calbuco eruptions, *Journal of Volcanology and Geothermal Research*, 361, 12–24, 2018.
- 880 Pfeiffer, T., Costa, A., and Macedonio, G.: A model for the numerical simulation of tephra fall deposits, *Journal of Volcanology and Geothermal Research*, 140, 273–294, 2005.
- Pouget, S., Bursik, M., Sparks, R., Hogg, A., Johnson, C., Singh, T., and Pavolonis, M.: Gravity current model of the volumetric growth of volcanic clouds: remote assessment with satellite imagery and estimation of mass eruption rate, in: *AGU Fall Meeting Abstracts*, 2013.
- Reckziegel, F., Folch, A., and Viramonte, J.: ATLAS-1.0: Atmospheric Lagrangian dispersion model for tephra transport and deposition, *Computers & Geosciences*, 131, 41–51, 2019.
- 885 Romero, J., Morgavi, D., Arzilli, F., Daga, R., Caselli, A., Reckziegel, F., Viramonte, J., Díaz-Alvarado, J., Polacci, M., Burton, M., et al.: Eruption dynamics of the 22–23 April 2015 Calbuco Volcano (Southern Chile): Analyses of tephra fall deposits, *Journal of Volcanology and Geothermal Research*, 317, 15–29, 2016.
- Rossi, E., Pollastri, S., and Bonadonna, C.: Ash aggregation in volcanic plumes: when, where, how. A new theoretical perspective., *EGUGA*, p. 12854, 2018.
- 890 Saltelli, A., Annoni, P., Azzini, I., Campolongo, F., Ratto, M., and Tarantola, S.: Variance based sensitivity analysis of model output. Design and estimator for the total sensitivity index, *Computer Physics Communications*, 181, 259 – 270, <https://doi.org/10.1016/j.cpc.2009.09.018>, <http://www.sciencedirect.com/science/article/pii/S0010465509003087>, 2010.
- Scollo, S., Tarantola, S., Bonadonna, C., Coltelli, M., and Saltelli, A.: Sensitivity analysis and uncertainty estimation for tephra dispersal models, *Journal of Geophysical Research-Solid Earth*, 113, 1–17, <https://doi.org/10.1029/2006JB004864>, 2008.
- 895 Sparks, R.: The dimensions and dynamics of volcanic eruption columns, *Bulletin of Volcanology*, 48, 3–15, 1986.
- Sparks, R. S. J., Bursik, M., Carey, S., Gilbert, J., Glaze, L., Sigurdsson, H., and Woods, A.: *Volcanic plumes*, Wiley, 1997.
- Suzuki, Y. and Koyaguchi, T.: A three-dimensional numerical simulation of spreading umbrella clouds, *Journal of Geophysical Research: Solid Earth*, 114, 2009.
- 900 Textor, C., Graf, H., Herzog, M., Oberhuber, J., Rose, W. I., and Ernst, G.: Volcanic particle aggregation in explosive eruption columns. Part II: Numerical experiments, *Journal of volcanology and geothermal research*, 150, 378–394, <http://www.sciencedirect.com/science/article/pii/S0377027305002994>, 2006a.
- Textor, C., Graf, H.-F., Herzog, M., Oberhuber, J. M., Rose, W. I., and Ernst, G. G.: Volcanic particle aggregation in explosive eruption columns. Part I: Parameterization of the microphysics of hydrometeors and ash, *Journal of volcanology and geothermal research*, 150, 359–377, <http://www.sciencedirect.com/science/article/pii/S0377027305002982>, 2006b.
- 905 Ungarish, M. and Huppert, H. E.: On gravity currents propagating at the base of a stratified ambient, *Journal of Fluid Mechanics*, 458, 283–301, 2002.



- Van Eaton, A. R., Amigo, Á., Bertin, D., Mastin, L. G., Giacosa, R. E., González, J., Valderrama, O., Fontijn, K., and Behnke, S. A.: Volcanic lightning and plume behavior reveal evolving hazards during the April 2015 eruption of Calbuco volcano, Chile, *Geophysical Research Letters*, 43, 3563–3571, 2016.
- 910
- Veitch, G. and Woods, A. W.: Particle aggregation in volcanic eruption columns, *Journal of Geophysical Research: Solid Earth*, 106, 26 425–26 441, 2001.
- Webster, H. N., Devenish, B. J., Mastin, L. G., Thomson, D. J., and Van Eaton, A. R.: Operational modelling of umbrella cloud growth in a lagrangian volcanic ash transport and dispersion model, *Atmosphere*, 11, 200, 2020.
- 915
- Woodhouse, M., Hogg, A., Phillips, J., and Sparks, R.: Interaction between volcanic plumes and wind during the 2010 Eyjafjallajökull eruption, Iceland, *Journal of Geophysical Research: Solid Earth*, 118, 92–109, 2013.
- Woods, A. W.: The fluid dynamics and thermodynamics of eruption columns, *Bulletin of Volcanology*, 50, 169–193, <http://www.springerlink.com/index/G4M430TG5X2H9J28.pdf>, 1988.
- Woods, A. W.: Moist convection and the injection of volcanic ash into the atmosphere, *Journal of Geophysical Research: Solid Earth*, 98, 920 17 627–17 636, 1993.